







# Mitochondrial rewiring with small-molecule drug-free nanoassemblies unleashes anticancer immunity

Received: 12 March 2024

Accepted: 22 August 2024

Published online: 03 September 2024

 Check for updates


Lulu Ren<sup>1,2</sup>, Jianqin Wan<sup>1</sup>, Xiaoyan Li<sup>1,3</sup>, Jie Yao<sup>1,3</sup>, Yan Ma<sup>1</sup>, Fanchao Meng<sup>1</sup>, Shusen Zheng<sup>1</sup>  , Weidong Han<sup>4</sup>   & Hangxiang Wang<sup>1,2,5</sup>  

The immunosuppressive tumor microenvironment (TME) remains a major obstacle to tumor control and causes suboptimal responses to immune checkpoint blockade (ICB) therapy. Thus, developing feasible therapeutic strategies that trigger inflammatory responses in the TME could improve the ICB efficacy. Mitochondria play an essential role in inflammation regulation and tumor immunogenicity induction. Herein, we report the discovery and characterization of a class of small molecules that can recapitulate aqueous self-assembly behavior, specifically target cellular organelles (e.g., mitochondria), and invigorate tumor cell immunogenicity. Mechanistically, this nanoassembly platform dynamically rewires mitochondria, induces endoplasmic reticulum stress, and causes apoptosis/paraptosis-associated immunogenic cell death. After treatment, stressed and dying tumor cells can act as prophylactic or therapeutic cancer vaccines. In preclinical mouse models of cancers with intrinsic or acquired resistance to PD-1 blockade, the local administration of nanoassemblies inflames the immunologically silent TME and synergizes with ICB therapy, generating potent antitumor immunity. This chemically programmed small-molecule immune enhancer acts distinctly from regular cytotoxic therapeutics and offers a promising strategy for synchronous and dynamic tailoring of innate immunity to achieve traceless cancer therapy and overcome immunosuppression in cancers.

Immunotherapy has revolutionized clinical cancer treatment. In particular, immune checkpoint blockade (ICB) antibodies targeting the immunoregulatory receptors programmed death 1 (PD-1), programmed death-ligand 1 (PD-L1), and cytotoxic T lymphocyte antigen 4 (CTLA-4) have had marked success against various human cancers<sup>1</sup>. However, only a small subset of patients responds to this therapy, and most of the partial responders eventually experience disease

progression due to tumor immune evasion<sup>2</sup>. The majority of barriers to effective T-cell based immunotherapy results from a myriad of factors, including insufficient tumor-infiltrating T lymphocytes (TILs), high immune suppressor contents, and low mutational burden<sup>3,4</sup>. Thus, a better understanding of the immune landscape of the tumor microenvironment (TME) offers new therapeutic strategies to reverse pro-tumor suppressive status and eventually unleash effector T cells.

<sup>1</sup>The First Affiliated Hospital, NHC Key Laboratory of Combined Multi-Organ Transplantation, Collaborative Innovation Center for Diagnosis and Treatment of Infectious Diseases, State Key Laboratory for Diagnosis and Treatment of Infectious Diseases, Zhejiang University School of Medicine, Hangzhou, Zhejiang Province, PR China. <sup>2</sup>Jinan Microecological Biomedicine Shandong Laboratory, Jinan, Shandong Province, PR China. <sup>3</sup>Department of Chemical Engineering, Zhejiang University, Hangzhou, Zhejiang Province, PR China. <sup>4</sup>Department of Colorectal Medical Oncology, Zhejiang Cancer Hospital, Hangzhou, Zhejiang Province, PR China. <sup>5</sup>Department of Hepatobiliary Surgery, The First Affiliated Hospital, Wenzhou Medical University, Wenzhou, Zhejiang Province, PR China.

 e-mail: [shusenzheng@zju.edu.cn](mailto:shusenzheng@zju.edu.cn); [hanwd@zjcc.org.cn](mailto:hanwd@zjcc.org.cn); [wanghx@zju.edu.cn](mailto:wanghx@zju.edu.cn)

Emerging strategies to address this substantial clinical challenge have focused on improving ICB therapy with additional immunostimulatory agents or by developing new combination treatments<sup>5–8</sup>.

Stressed and dying cancer cells emit numerous immunostimulatory molecules, including small metabolites, antigens, cytokines, and damage-associated molecular patterns (DAMPs). These signaling bioactive components interact with the host immune system and collaborate with adaptive immune responses to induce anticancer immunity<sup>9</sup>. Accumulating preclinical and clinical evidence demonstrates that certain chemotherapy regimens can trigger inflammatory innate immune responses by releasing stimulatory molecules from dying cancer cells<sup>10</sup>. Indeed, inducing immunogenic cell death (ICD) with various approved chemotherapy regimens has been pursued in the clinic to improve immunotherapy outcomes<sup>11,12</sup>. Moreover, considerable effort has been dedicated to combine these chemotherapies with T-cell based immunotherapy to control tumor progression<sup>13</sup>. However, the substantial toxicity of current chemotherapy treatments warrants the development of alternative immunogenic strategies; such treatments would benefit large populations of patients with cancer. Mitochondria, the indispensable cellular organelles for energy supply, are essential for cellular metabolism and can sustain cancer growth and progression<sup>14</sup>. Research suggests that mitochondria are the powerhouses of immunity<sup>15,16</sup>. Hence, selective mitochondria-targeting and intervention strategies could suppress cancer by eliciting tumor cell immunogenicity, eventually activating reactive effector T cells and enhancing their infiltration in tumors<sup>17–20</sup>.

In this study, we develop dynamic nanoassemblies constructed from self-assembling nontherapeutic small molecules and engineer this nanoplatform to specifically target cellular organelles (e.g., mitochondria) to rewire mitochondria and enhance tumor immunogenicity (Fig. 1). We delineate a series of lipid conjugates by the covalent ligation of structurally diverse fatty acids and a mitochondria-targeting moiety, 3-(aminopropyl)triphenylphosphonium (TPP). These conjugates are capable of recapitulating self-assembly behavior to form well-defined nanostructures and potentiate tumor immunogenicity. This class of synthetic nondrug immune enhancer could provide a powerful approach to overcome immunosuppression in solid tumors.

## Results

### Lipid conjugation induces supramolecular self-assembly and aggregation-induced cytotoxicity

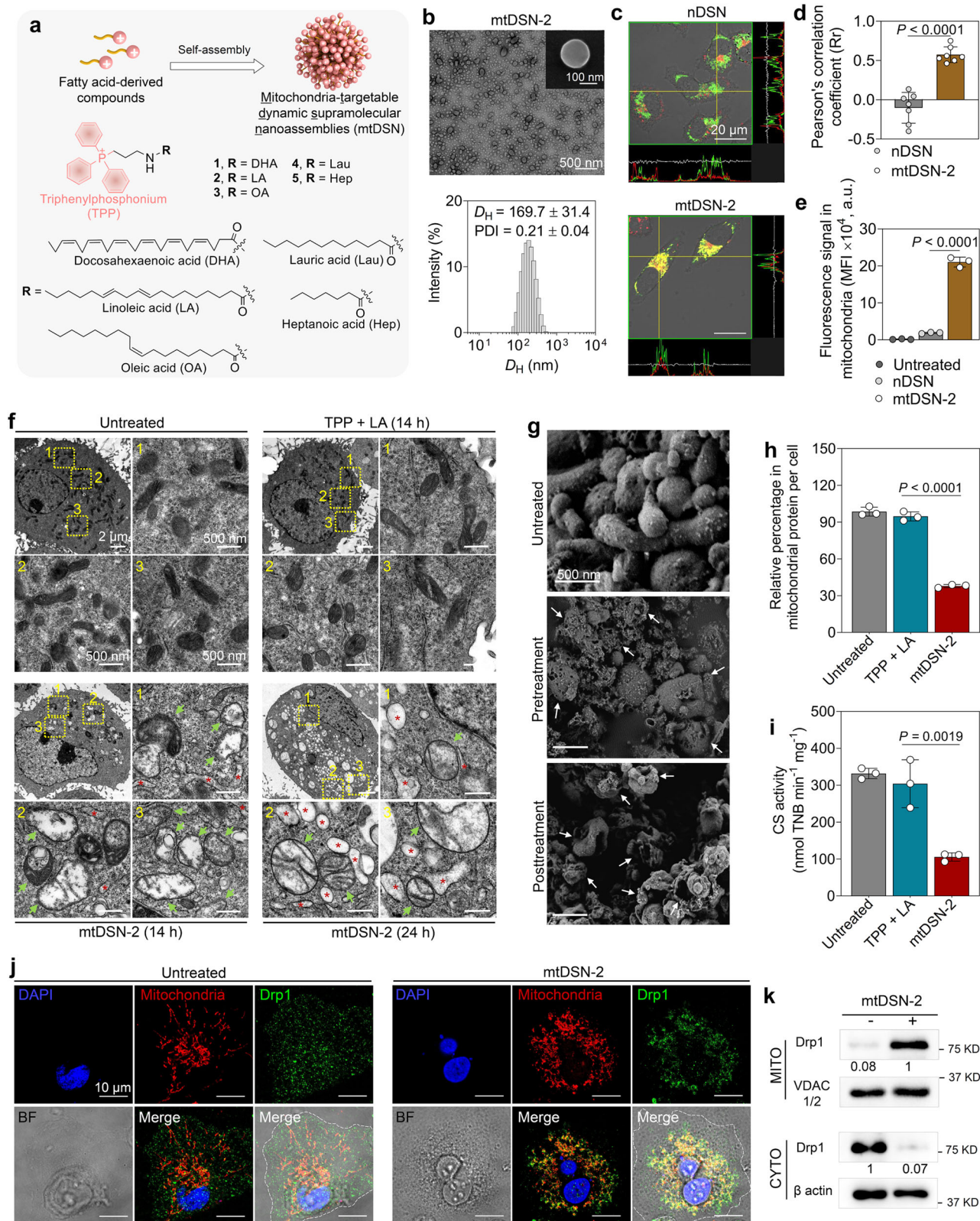
We previously have shown that the covalent conjugation of therapeutic agents with fatty acids via a cleavable linker facilitates the supramolecular self-assembly and in vivo delivery of structurally diverse small molecular therapeutics<sup>21–24</sup>. Here, to expand the repertoire of this approach, we generated a class of self-assembling chemical inducers using fatty acid-based conjugation and evaluated their mitochondria-targeting and function rewiring abilities. We used polyunsaturated (e.g., docosahexaenoic acid (DHA) and linoleic acid (LA)), monounsaturated (e.g., oleic acid (OA)), and saturated (e.g., lauric acid (Lau) and heptanoic acid (Hep)) fatty acids for TPP conjugation (Fig. 1a). We confirmed the chemical structures and purities of the resultant conjugates by <sup>1</sup>H and <sup>13</sup>C nuclear magnetic resonance spectroscopy and high-resolution mass spectrometry (Supplementary Figs. 1–5). Moreover, all of the conjugates were structurally stable in dimethyl sulfoxide (DMSO) for at least 60 days when stored at –20 °C (Supplementary Fig. 6). Next, we examined the self-assembly behavior of these TPP-derived lipids by slowly injecting them as DMSO solutions into deionized water. Intriguingly, all of the five TPP derivatives formed spherical nanostructures, as observed by transmission electron microscopy (TEM) (Fig. 1b and Supplementary Fig. 7a). Dynamic light scattering revealed that the hydrodynamic diameters of these nanoassemblies were 45 to 170 nm (Fig. 1b and Supplementary Fig. 7a). As expected, the surface zeta potential was positive (Supplementary Fig. 7b), attributing to the positive charge in the TPP moiety.

Unexpectedly, the lipid nanoassemblies decimated cancer cells. This observation inspired us to evaluate their cytotoxicity across a panel of distinct cancer cell lines, including cisplatin-resistant cancer cells. Strikingly, these lipid nanoassemblies had more potent cytotoxicities and lower median inhibitory concentrations (IC<sub>50</sub>) than clinically approved cisplatin, especially in refractory cancer cells (Supplementary Table 1). In stark contrast, treatment with either the TPP moiety or fatty acids alone, or with a simple mixture of both, exhibited low cytotoxicity and demonstrated negligible effects on cell viability (Supplementary Table 2). These data suggest that the cytotoxic mechanism of nanoassemblies is distinct to that of cisplatin and mitigates cisplatin-induced resistance. In subsequent experiments, we used the nanoassemblies derived from the TPP-LA conjugate **2** that was thermodynamically stable (Supplementary Fig. 8) and was superior in terms of cytotoxic potency.

### Trafficking of nanoassemblies to mitochondria causes lethal mitochondrial dysfunction

Intrigued by the strong cytotoxicity, we first endeavored to explore intracellular fate of these nanoassemblies. For this purpose, we labeled conjugate **2**-assembled nanoparticles with a linoleic acid-tethered fluorescent dye, Cy5.5 (Supplementary Fig. 9a and b). We observed that the cellular uptake of these nanoparticles is energy-dependent, as lowering the temperature impeded their internalization (Supplementary Fig. 9c). Detailed inhibitor co-incubation assays revealed that the nanoassemblies predominantly entered cells through macropinocytosis and clathrin-dependent endocytosis; blocking these pathways with specific inhibitors significantly reduced their internalization (Supplementary Fig. 9d). Confocal laser scanning microscopy (CLSM) demonstrated that the nanoassemblies initially localized within endo/lysosomal compartments before escaping (Supplementary Fig. 9e). Owing to the conjugation of the TPP motif, we wondered whether the nanoassemblies could subsequently target intracellular mitochondria. CLSM observation showed that the labeled nanoassemblies overlapped well with MitoTracker Green in mitochondria (with a high Pearson's colocalization coefficient of 0.6, Fig. 1c and d) rather than endoplasmic reticulum (ER) (Supplementary Fig. 9f), suggesting that the nanoassemblies specifically self-localized to mitochondria in cells. Hence, we named these mitochondria-targetable dynamic supramolecular nanoassemblies as mtDSN. By contrast, nanoassemblies lacking the TPP ligand lost the organelle specificity and were distributed throughout the cytoplasm (Fig. 1c). We then isolated mitochondria from cells and performed flow cytometry analysis to examine the mitochondrial accumulation of mtDSN-2 (Fig. 1e). In accordance with the CLSM results, mtDSN-2 displayed substantially more localization in mitochondria than the nontargetable nanoassemblies.

Next, we investigated how mtDSN-2 impacted the mitochondrial ultrastructure. In HeLa/R cells exposed to the physical mixture of TPP and linoleic acid, mitochondria presented a well-arranged thread-like structure with clear double membranes, similar to those of untreated cells (Fig. 1f). By sharp contrast, mtDSN-2 treatment caused abnormal mitochondrial ultrastructure expanding to nearly spherical structures with evident collapse of the intracristae compartment and substantial matrix swelling (Fig. 1f)<sup>25</sup>. Mitochondrial damages similar to that observed in HeLa/R cells were also evident in mtDSN-2-treated 4T1 cells (Supplementary Fig. 10). We then carefully extracted mitochondria and observed their morphology by scanning electron microscopy (SEM) (Fig. 1g). Compared with the thread-like mitochondria with intact membrane in the untreated cells, mtDSN-2 exposure led to numerous irregularly shaped holes in the mitochondrial membrane. Some mitochondria were even fragmented, with only gross mitochondrial morphology dimly preserved. Strikingly, we also observed mitochondria with huge cavities and warped configuration after directly adding mtDSN-2 on isolated mitochondria (Fig. 1g



bottom). Besides, mtDSN-2 treatment significantly reduced total mitochondrial proteins and citrate synthase activity, indicating dampened mitochondrial biogenesis (Fig. 1h, i)<sup>26</sup>. Specifically, mitochondrial dynamics investigation revealed enhanced mitochondrial fission, as evidenced by the recruitment of dynamin-related protein 1 (Drp1) clusters from the cytoplasm to the mitochondrial membrane following mtDSN-2 treatment (Fig. 1j, k)<sup>27,28</sup>.

### mtDSN triggers mitochondria-associated paraptosis and apoptosis

Next, we sought to identify the forms of programmed cell death triggered by mtDSN-2 treatment. Fatty acids are known to cause ferroptosis, where lipid peroxidation commonly occurs<sup>29</sup>. Although we detected byproducts (e.g., malondialdehyde (MDA) and 4-hydroxynonenal (4-HNE)) of mitochondrial lipid peroxidation after mtDSN-2 exposure

**Fig. 1 | Mitochondria-targetable dynamic supramolecular nanoassemblies (mtDSN) induce mitochondrial dysfunction.** **a** Chemical structures of fatty acid-TPP conjugates and schematic of the self-assembly of these small molecules. **b** Representative TEM image (inset: SEM image) and size distribution of linoleic acid-derived mtDSN (mtDSN-2).  $D_H$ , hydrodynamic diameter. PDI, polydispersity index. **c** Confocal microscopy images showing the colocalization of mtDSN-2 with mitochondria upon cellular uptake. The corresponding fluorescence intensity profile analysis of marked positions (yellow crossed lines) is shown on the right and below the images. A nontargetable nanoassembly (nDSN) was included for comparison. Mitochondria: MitoTracker Green (green), DSN: Cy5.5 label (red). **d** Pearson's correlation coefficient (Rr) analysis of (c). **e** Mitochondrial accumulation of dye-labeled nanoassemblies detected by flow cytometry. MFI, mean fluorescence intensity. a.u., arbitrary unit. **f** TEM images of mitochondrial ultrastructures after different treatments in HeLa/R cancer cells. Green arrows and red asterisks indicate the damaged mitochondria and swelling endoplasmic reticulum, respectively. **g** SEM images of isolated mitochondria from cancer cells. Pretreatment: cells were pretreated with 5  $\mu$ M mtDSN-2 for 12 h before mitochondria extraction.

Posttreatment: mitochondria were recovered from cells and then incubated with 0.5  $\mu$ M mtDSN-2 for 30 min at 4 °C. Arrows indicate damaged mitochondria. **h** Relative protein content in mitochondria per cell in each treatment. **i**, Citrate synthase (CS) activity in mitochondria after each treatment, determined by measuring the production of 2-nitro-5-thiobenzoic acid (TNB). **j** Immunofluorescence staining revealed the recruitment of the Drp1 protein to mitochondria in response to mtDSN-2 treatment. Mitochondria: MitoTracker Red CMXRos (red), Drp1: antibody against Drp1 (green), nuclei: DAPI (blue), BF: bright field. **k** Drp1 levels in mitochondria (MITO) and cytosol (CYTO), assessed by immunoblotting. Band intensities were quantitatively analyzed from the 8-bit digital images by densitometry in ImageJ. The data are presented as the mean  $\pm$  s.d.  $n = 3$  biologically independent samples (**b–c**, **e–j**). Data of seven different views from three biologically independent samples (**d**). The similar results were repeated in two biologically independent experiments (**k**). Statistical analysis by Student's *t* test (**d**) or one-way ANOVA with Turkey's multiple comparisons test (**e**, **h** and **i**). Source data are provided as a Source data file.

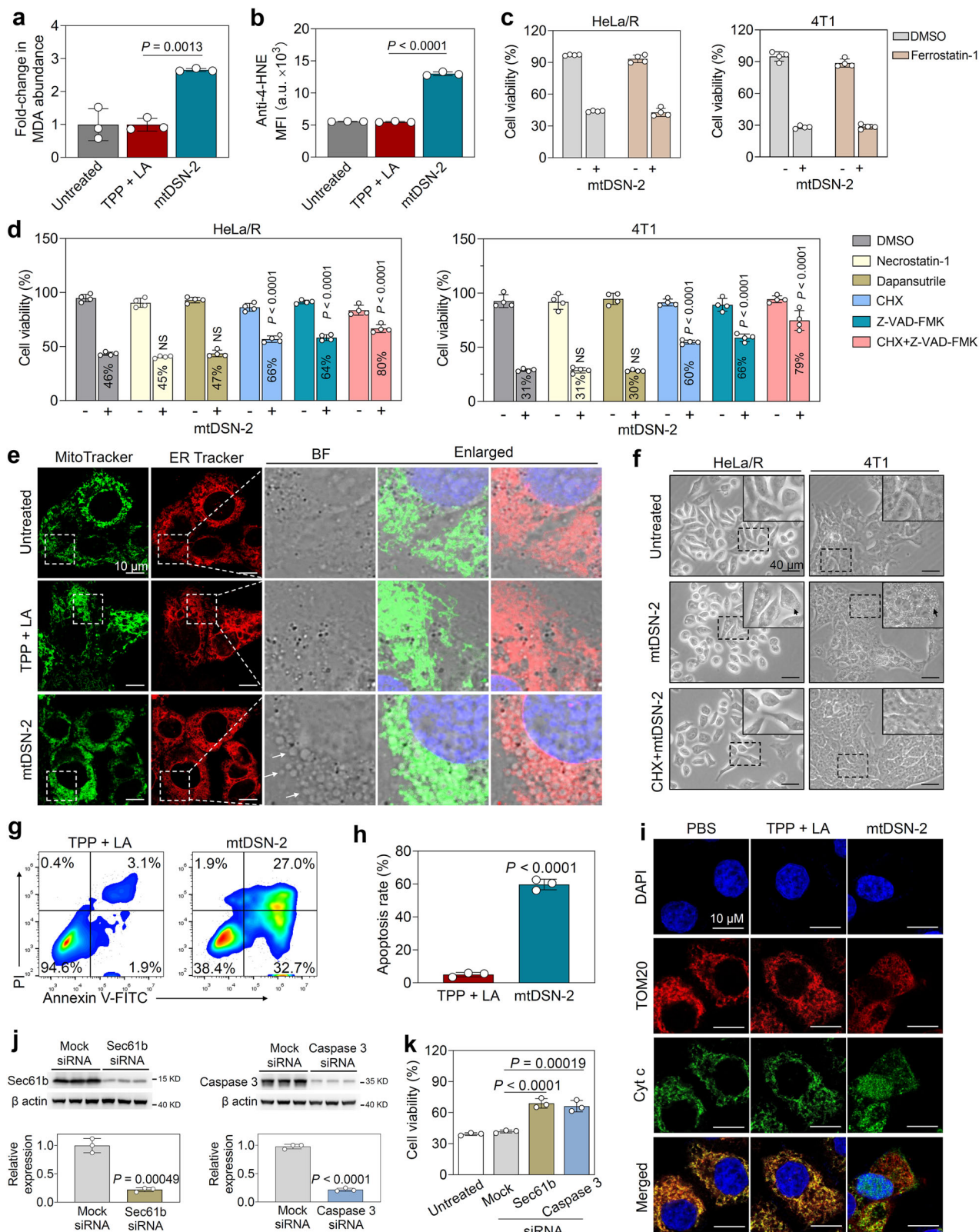
(Fig. 2a and b), pretreating the cells with ferrostatin-1, a ferroptosis inhibitor, did not affect cell viability (Fig. 2c). In addition, inhibiting necroptosis or pyroptosis pharmacologically also failed to rescue the viability of cancer cells (Fig. 2d). These data suggested that mtDSN-2 did not exert cytotoxicity by triggering ferroptosis, necroptosis, or pyroptosis. Furthermore, using the de novo translation inhibitor cycloheximide (CHX) for paraptosis or pan-caspase inhibitor z-VAD for apoptosis improved cell survival, suggesting a mitochondrial paraptosis/apoptosis mechanism. Paraptosis is a de novo translation-dependent form of cell death featured by extensive cytoplasmic vacuolation due to mitochondria and endoplasmic reticulum (ER) swelling<sup>30,31</sup>. Indeed, mtDSN-2-exposed cells displayed these typical morphological features (Figs. 1f, 2e, Supplementary Fig. 10 and 11). Furthermore, the paraptosis inhibitor (CHX) reversed mtDSN-induced cytoplasmic vacuolation (Fig. 2f). A flow cytometry analysis confirmed that, besides paraptosis, mtDSN-2 induced apoptosis in a dose-dependent manner (Fig. 2g, h, Supplementary Fig. 12a and b). Consistently, the western blot analysis showed the activation of caspase 9 and 3 as well as poly(ADP-ribose) polymerase (PARP), suggesting an irreversible progression of apoptosis (Supplementary Fig. 12c). Analysis of Bcl-2 family proteins, which are involved in mitochondria-associated apoptosis, confirmed that mtDSN-2 did not affect the expression of Bcl-2, Bim, and Bax. However, we observed an obvious translocation of proapoptotic Bax from the cytoplasm to the outer mitochondrial membrane<sup>32,33</sup> in response to mtDSN-2 (Supplementary Fig. 12d). The redistribution of cytochrome c is considered an important hallmark of apoptosis<sup>34</sup>. As expected, mtDSN-2 treatment readily induced cytochrome c release from mitochondria into the cytoplasm and nuclear region (Fig. 2i). Sec61b and caspase 3 are crucial in mediating paraptosis and apoptosis, respectively<sup>31,35,36</sup>. Intriguingly, we found that silencing Sec61b and caspase 3 inhibited the mtDSN-2-induced cell death (Fig. 2j, k, and Supplementary Fig. 13). This finding further supports the proposed mechanism by which mtDSN-2 induces lethal mitochondrial paraptosis/apoptosis.

### mtDSN enhances tumor immunogenicity via fostering ICD cascade

Accumulating evidence shows that focused mitochondrial and/or ER damage produces proinflammatory effects by evoking abundant and large-scale ICD<sup>9</sup>. Thus, we first examined whether mtDSN-2 could trigger the ICD cascade. We analyzed the externalized calreticulin (ecto-CRT) on the cancer cell membrane, which is an “eat me” signal for phagocytes and an ICD-relevant indicator<sup>11,37</sup>. As shown in Fig. 3a, b and Supplementary Fig. 14, mtDSN-2 treatment induced a massive CRT translocation from the ER to the cell membrane. Western blot analysis of purified plasma membrane also confirmed the CRT externalization (Fig. 3c). We also investigated high mobility group protein B1 (HMGB1)

and ATP release, the hallmarks of ICD<sup>38,39</sup>. mtDSN-2 caused a significant HMGB1 release from the nucleus to the cytoplasm and extracellular medium in both tested cancer cell lines (Fig. 3d, e). Moreover, mtDSN-2 sharply reduced the intracellular ATP concentration while promoting its extracellular secretion (Fig. 3f, g). These results indicate that mtDSN-2 performs like certain ICD-inducing chemotherapy (e.g., doxorubicin and oxaliplatin), evoking a bona fide ICD cascade in cancer cells, probably releasing sufficient tumor-associated antigens and DAMPs. These secreted DAMPs are crucial for the recognition and engulfment of dying cancer cells by dendritic cells, which favors dendritic cell activation. Hence, we investigated whether mtDSN-2-treated cancer cells could boost dendritic cell maturation in vitro. We exposed bone marrow-derived dendritic cells (BMDC) freshly isolated from mice to culture medium from different pretreated tumor cells, and counted the matured dendritic cells (CD11c<sup>+</sup>CD80<sup>+</sup>CD86<sup>+</sup>) by flow cytometry. The physical mixture of TPP plus linoleic acid did not promote dendritic cell maturation, while mtDSN-2 pretreatment increased the proportions of mature dendritic cells by 1.7- and 1.9-fold in 4T1 and HeLa/R cells, respectively (Fig. 3h and Supplementary Fig. 15). In addition, the expression of major histocompatibility complex II (MHCII) was coincidentally upregulated in dendritic cells, confirming that mtDSN-2 caused immune activation (Fig. 3i).

To clarify the mtDSN-2-induced ICD mechanism, we examined reactive oxygen species (ROS) production and ER stress, as they are essential prerequisites for ICD induction<sup>9</sup>. Mitochondrial damage is generally accompanied by excessive ROS generation. Using the mitochondria-specific probe MitoSOX, we found that mtDSN-2 significantly increased mitochondrial superoxide levels in cancer cells compared with other treatments (Fig. 3j, k). Furthermore, using 2',7'-dichlorofluorescein diacetate (DCFH-DA), we confirmed that mtDSN-2-treated cells had remarkably higher ROS intracellular levels than other cells (Supplementary Fig. 16). Electron cryo-microscopy observation has previously unveiled that the ER and mitochondria are tightly juxtaposed and that substance and signaling transportation occurs through membrane contact sites<sup>40,41</sup>. Thus, we wondered whether mitochondria perturbation and overloading of ROS could lead to ER dysfunction and stress. Flow cytometry analysis (Fig. 3l, m) and CLSM observation (Fig. 3n) revealed ER mass enlargement and swelling in cells exposed to mtDSN-2, indicating notable ER perturbation. Subsequently, the loss of ER proteostasis was also observed, evidenced by an increase in ubiquitinated proteins in mtDSN-2-treated cells (Supplementary Fig. 17)<sup>42</sup>. We further quantified ER stress-related marker proteins in these cell lines by western blot. mtDSN-2 augmented the phosphorylation of protein kinase RNA-like ER kinase (PERK) and eukaryotic translation initiation factor 2 $\alpha$  (eIF2 $\alpha$ ), and increased the expression levels of activating transcription factor 4 (ATF4) and proapoptotic C/EBP homologous protein (CHOP) (Fig. 3o). Cell immunofluorescence



staining confirmed the pronounced upregulation of CHOP expression after mtDSN-2 treatment (Fig. 3p). Intriguingly, mtDSN-2 treatment also activated and phosphorylated heme-regulated eIF2a kinase (HRI), another member of the eIF2a kinase family (Fig. 3o). Recent studies showed that HRI mediated eIF2a phosphorylation in the integrated stress response triggered by mitochondrial dysfunction<sup>43</sup>. Since eIF2a phosphorylation is required for CRT externalization on the cell

surface<sup>44</sup>, mtDSN-2 probably sparked ICD via inducing eIF2a phosphorylation in a PERK- and HRI-dependent pattern.

### mtDSN-2-pulsed tumor cells are immunogenic and serve as prophylactic vaccine

The ICD induction by mtDSN-2 *in vitro* motivated us to assess whether mtDSN-2 could promote tumor immunogenicity *in vivo* by

**Fig. 2 | mtDSN induces cell death in an apoptosis and paraptosis-dependent manner.** **a** Assessment of lipid peroxidation by quantifying intracellular malondialdehyde (MDA). **b** Anti-4-HNE lipid peroxidation staining in tumor cells detected by flow cytometry. a.u., arbitrary units. **c** and **d**, Cell viability of Hela/R and 4T1 cells pretreated with ferroptosis inhibitor Ferrostatin-1 (10  $\mu$ M), necroptosis inhibitor Necrostatin-1 (10  $\mu$ M), pyroptosis NLRP3 inhibitor Dapansutrile (10  $\mu$ M), paraptosis inhibitor cycloheximide (CHX, 10  $\mu$ M), or pan-caspase apoptosis inhibitor Z-VAD-FMK (40  $\mu$ M) before incubation with or without mtDSN-2. *P* indicates the significance relative to DMSO treatment. **e** Confocal microscopy images of 4T1 cells showing cytoplasmic vacuolization (indicated by white arrows) after mtDSN-2 treatment. Mitochondria: MitoTracker Green (green), endoplasmic reticulum: ER Tracker Red (red), nuclei: Hoechst 33342 (blue), BF: bright field. **f** Cell morphology after exposure to mtDSN-2 in the presence or absence of CHX. Black

arrows indicate cytoplasmic vacuolization. **g** and **h**, Flow cytometry analysis of cell apoptosis after TPP + LA (20  $\mu$ M) or mtDSN-2 (10  $\mu$ M) treatments for 48 h. **i**, Immunofluorescence analysis of mtDSN-2-triggered release of cytochrome c (Cyt c) from mitochondria into the cytosol and nuclear region. Mitochondria: antibody against TOM20 (red), Cyt c: antibody against Cyt c (green), nuclei: DAPI (blue). **j** Immunoblotting analysis and quantification of 4T1 cells transfected with mock (untargeted), Sec61b or caspase 3 siRNA. **k** Cell viability of 4T1 cells transfected with mock, Sec61b or caspase 3 siRNA followed by exposure to mtDSN-2. The data are presented as the mean  $\pm$  s.d. The results were shown from three biologically independent experiments (**a–b** and **e–k**). *n* = 4 biologically independent samples in two cell lines (**c** and **d**). NS: not significant. Statistical analysis by Student's *t* test (**h**, **j**) or one-way ANOVA with Turkey's multiple comparisons test (**a**, **b**, **d** and **k**). Source data are provided as a Source data file.

investigating the prophylactic vaccination response in immunocompetent BALB/c mice. Certain chemotherapeutic agents (e.g., doxorubicin) stimulate immune-dependent antitumor responses by inducing ICD and secreting numerous bioactive molecules—including DAMPs—that interact with the immune system<sup>45,46</sup>. Therefore, we exposed murine 4T1 cancer cells to mtDSN-2 or chemotherapy (doxorubicin or non-ICD drugs, i.e., paclitaxel and cisplatin), and vaccinated mice with a subcutaneous injection of dying cells into the right flank. Two weeks later, we orthotopically injected live 4T1 cells to assess the immune protection from tumorigenesis provided by the vaccination regimen (Fig. 4a). We interpreted the rejection of the orthotopic tumor growth as a sign of antitumor vaccination. Mice immunized with doxorubicin- or mtDSN-2-pretreated 4T1 cells displayed better cancer cell rejection features than other mice, namely a high tumor-free rate and extended survival (Fig. 4b, c). 4T1 breast cancer is poorly immunogenic but highly invasive and metastatic to distant organs. Interestingly, vaccination with mtDSN-2-exposed cells significantly restrained the metastatic burden to draining lymph nodes as well as to distal lung and liver (Fig. 4d, e and Supplementary Fig. 18).

To better understand the mechanism of mtDSN-mediated immunization, we examined the activation of immunological responses. Specifically, we looked at the T-cell activation-associated cytokines interleukin 12 (IL-12), tumor necrosis factor  $\alpha$  (TNF- $\alpha$ ), and interferon  $\gamma$  (IFN- $\gamma$ ) by enzyme-linked immunosorbent assay (ELISA) before and after vaccination. The immunization with mtDSN-2-treated tumor cells significantly increased the levels of these cytokines compared with conventional paclitaxel or cisplatin regimens (Fig. 4f). Dendritic cell maturation plays a pivotal role in antigen presentation to T lymphocytes, and initiates adaptive immunity response<sup>10</sup>. Flow cytometry analysis of the tumor-draining lymph nodes indicated that mtDSN-2 vaccination facilitated dendritic cell maturation, increasing the frequency of CD11c<sup>+</sup>CD80<sup>+</sup>CD86<sup>+</sup> cells from 9.9% (in saline-treated mice) to 34.8%. The proportion of MHC II<sup>+</sup> dendritic cells also increased by 2.4 folds (Fig. 4g and Supplementary Fig. 19). Moreover, the mtDSN-2- and doxorubicin-treated cancer cell-based vaccines converted naive T cells to the active phenotype and to the effector memory T-cell (T<sub>EM</sub>) phenotype (CD3<sup>+</sup>CD4/8<sup>+</sup>CD62L<sup>-</sup>CD44<sup>+</sup>) in vivo (Fig. 4h and Supplementary Fig. 20). These results suggest that mtDSN-2-treated cancer cell-based vaccination generated T-cell memory response in mice, accounting for the long-term rejection of rechallenged viable tumor cells.

### Intratumoral injection of mtDSN induces abscopal antitumor effect

Encouraged by the cancer vaccine effect, we next tested whether local mtDSN treatment could elicit abscopal antitumor immune responses against distant tumor lesions. To this end, we established a bilateral 4T1 tumor model in BALB/c mice, and only treated the primary tumor with mtDSN (Fig. 5a). Two intratumoral injections of mtDSN-2 to the right flank tumors significantly inhibited the growth of both the treated and untreated tumors (Fig. 5b, c) and improved mouse survival

(Fig. 5d). Immunofluorescence staining also evidenced the expansion of tumor-infiltrating CD8<sup>+</sup> T cells at contralateral tumors after mtDSN-2 treatment compared with saline-treated mice, supporting the induction of a systemic immune response by mtDSN-2 (Fig. 5e). mtDSN therapy was well tolerated and showed negligible toxicity (Fig. 5f). To probe the specificity of the T-cell responses, we used unrelated CT26 colorectal cancer cells instead of 4T1 breast cancer cells as the contralateral tumor (Fig. 5g). In that case, mtDSN-2 suppressed the local tumor (Fig. 5h) but exerted no abscopal tumor control, as contralateral CT26 tumors displayed rapid growth kinetics comparable to those of saline-treated mice (Fig. 5i). These results indicate that tumor-specific immunity is responsible for the observed antitumor activity.

Cytotoxic CD8<sup>+</sup> T lymphocytes (CTL) are crucial for the abscopal effect. To further explore the specificity of mtDSN-mediated T-cell priming, we analyzed the CTL status in both TME and spleens in ovalbumin (OVA)-expressing or OVA-negative B16F10 mouse models (Fig. 5j). mtDSN-2 therapy increased the frequency of OVA<sub>257-264</sub> (SIINFEKL)-specific tumor-infiltrating CD8<sup>+</sup> T-cell expansion (detected using H-2K<sup>b</sup>-OVA tetramer staining) than saline treatment (Fig. 5k and Supplementary Fig. 21). As expected, mtDSN-2 treatment produced almost no OVA-specific CD8<sup>+</sup> T cells in OVA-deficient B16F10 tumors, demonstrating the stimulated OVA-specific T-cell responses (Fig. 5k). Moreover, B16F10-OVA tumors displayed higher frequencies of IFN- $\gamma$ -secreting OVA tetramer<sup>+</sup> CTLs than B16F10 tumors did after mtDSN-2 vaccination, further highlighting the potential of mtDSN as an in situ vaccine for priming effector T-cell responses (Fig. 5l, m). CTL profiling of splenocytes also supported the results observed in the TME (Fig. 5n, o). Together, these results support the premise that the mtDSN scaffold initiates ICD-induced tumor-specific T-cell activation, thereby driving abscopal antitumor immunity.

### mtDSN-2 synergizes with immunotherapies to control tumor growth

Toll-like receptors are pattern recognition receptors that play a fundamental role in activating innate immunity<sup>47</sup>. The TLR4 agonist monophosphoryl lipid A (MPLA) is a lipopolysaccharide derivative that can serve as an adjuvant enhancing the efficacy of cancer treatments<sup>48</sup>. The intratumoral combination of mtDSN-2 with MPLA improved the tumor-suppressive effect (Fig. 6a) and mouse survival extension (Fig. 6b) of mtDSN-2 monotherapy, and led to abundant infiltration of CD8<sup>+</sup> T cells in subcutaneous 4T1 tumors (Fig. 6c). Additionally, mtDSN-2 synergized with clinically used ICB therapy (e.g., anti-PD-1 antibody) (Fig. 6a–c). The histological analysis of mouse lungs revealed that mtDSN-2 alone or combined with anti-PD-1 significantly attenuated metastatic tumor burden, as shown by the markedly low numbers of metastatic foci (Fig. 6d, e and Supplementary Fig. 22). However, the combination with MPLA was less efficient than that with anti-PD-1 for inhibiting tumor metastasis (Fig. 6d, e). Previous studies suggested a link between TLR4 activation and augmented metastatic phenotypes of cancer cells<sup>49</sup>. TLR4 activation also was associated with local and systemic inflammation, creating the TME (e.g., reconstructed

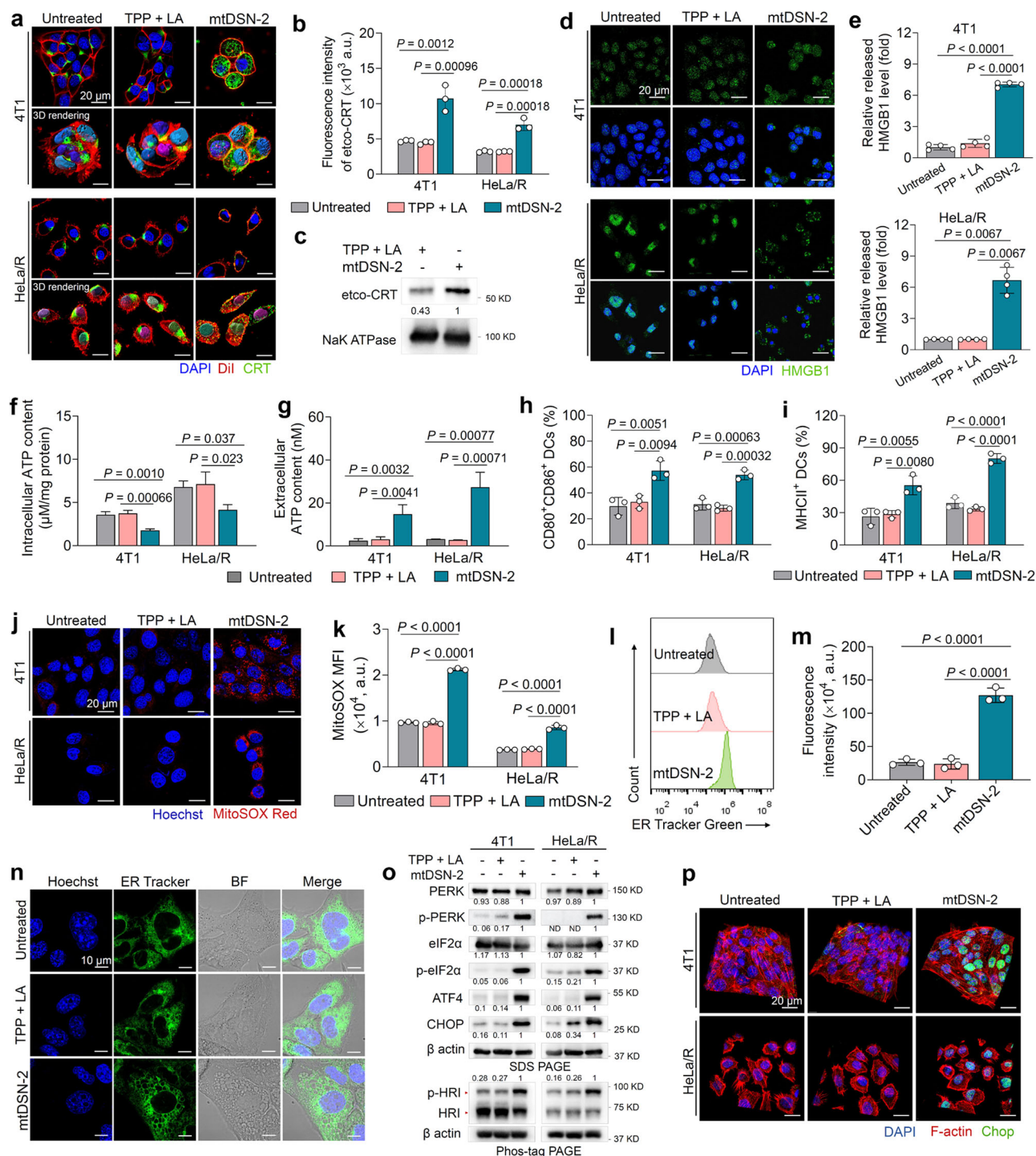
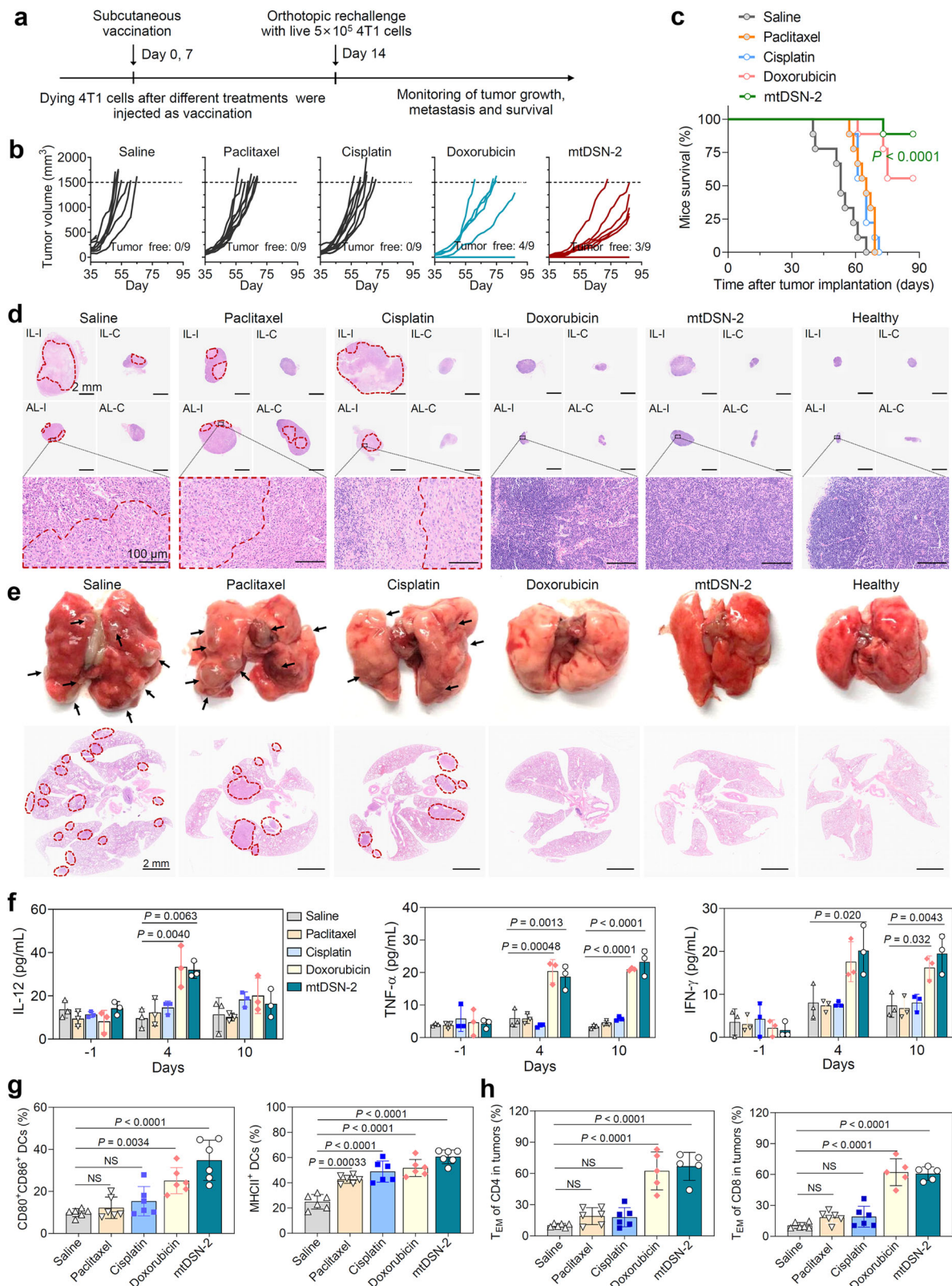


**Fig. 3 | mtDSN-2 incites ICD cascade related to cellular stress. a** Representative confocal microscopy images showing externalized CRT on the cell membrane after mtDSN-2 exposure. Cell membrane: Dil (red), CRT: antibody against CRT (green), nuclei: DAPI (blue). **b** The CRT exposure to cell surface was examined by immunofluorescence cytometry among viable cells (propidium iodide-negative). **c** Immunoblotting detection of CRT in the plasma membrane protein fraction. **d** Confocal microscopy images showed HMGB1 release from the nucleus to the cytoplasm after mtDSN-2 treatment. HMGB1: antibody against HMGB1 (green), nuclei: DAPI (blue). **e** Extracellular HMGB1 release determined by ELISA. Changes in intracellular (**f**) and extracellular (**g**) ATP content following different treatments. **h, i** Flow cytometry analysis of BMDC maturation after treatments (gated on CD11c<sup>+</sup> dendritic cells). Confocal microscopy (**j**) and flow cytometry (**k**) analysis of mitochondrial ROS production in tumor cells by MitoSox staining. Mitochondrial Superoxide: MitoSox Red (red), nuclei: Hoechst 33342 (blue). **l, m** Flow cytometry analysis showing ER Tracker Green in 4T1 cells. **n** ER swelling-related cytoplasmic

vacuolation assessed by confocal microscopy. **o** Western blot analysis of ER-stress related protein in cells treated with mtDSN-2 (5  $\mu$ M for 36 h). In the phos-tag PAGE assay, a phos-tag gel was used to resolve the protein phosphorylation, which can be assessed by the mobility shift. Band intensities were quantified from the 8-bit digital images by densitometry in ImageJ and are shown normalized to the mtDSN-2 lane for each target. ND, not detected. **p** Confocal microscopy images showing CHOP expression in tumor cells after different treatments. CHOP: antibody against CHOP (green), F-actin: Rhodamine Phalloidin (red), nuclei: DAPI (blue). a.u., arbitrary units. The data are presented as the mean  $\pm$  s.d. The representative images of panels (**a, d, j, and p**) were repeated in two biologically independent cell lines.  $n = 3$  biologically independent experiments (**b, f, i, and k–n**).  $n = 4$  biologically independent samples (**e**). The similar results were repeated in two biologically independent experiments (**c, o**). Statistical analysis by one-way ANOVA with Turkey's multiple comparisons test. Source data are provided as a Source data file.



tumor-associated lymphatic and blood vessels) that favors tumor recurrence and metastasis<sup>50,51</sup>. Hence, these effects of TLR4 agonist MPLA may account for the impaired metastatic inhibition of mtDSN-2.

Having shown this synergy, we then assessed the effect of mtDSN-2 against a murine colorectal cancer MC38 tumor model established in syngeneic C57BL/6 mice. This model is generally considered hypermutated and harbors a microsatellite-unstable phenotype, contributing

to a T-cell-inflamed TME<sup>52</sup>. Three intraperitoneal doses of anti-PD-1 antibody indeed notably dampened tumor growth, and four out of nine treated mice showed complete MC38 tumor regression, indicating robust ICB therapy responses (Fig. 6f, g). Treatment with mtDSN-2 induced tumor regression and, even more encouragingly, synergized with the PD-1 blockade, yielding highly potent antitumor activity. The combination therapy cured 89% of the mice, with tumor remission



**Fig. 4 | mtDSN-2 incites tumor immunogenicity against tumor relapse and metastases in vivo.** **a** Schedule of the prophylactic vaccination model in BALB/c mice to investigate the ICD-induced immunogenicity in vivo. **b** Individual tumor growth curves in each group ( $n = 9$  mice/group). Mice were sacrificed when tumor volume exceeded  $1500 \text{ mm}^3$ . **c** Kaplan–Meier survival curves of rechallenged mice after different vaccinations ( $n = 9$  mice/group).  $P$  indicates the statistical significance relative to the saline-treated group. Hematoxylin and eosin (H&E) staining revealed tumor metastases to lymph nodes (**d**) and lungs (**e**) from mice bearing established 4T1 tumors in each group on day 59. Red dotted regions and black arrows indicate metastasized tumors. IL-1 ipsilateral inguinal lymph nodes, IL-C contralateral inguinal lymph nodes, AL-1 ipsilateral axillary lymph nodes, AL-C

contralateral axillary lymph nodes.  $n = 3$  mice/group. Analysis of immune landscape after vaccination. Levels of IL-12, TNF- $\alpha$  and IFN- $\gamma$  in the serum of mice on the indicated days (**f**,  $n = 3$  biologically independent samples); quantitative analyses of mature dendritic cells (CD45<sup>+</sup>CD11c<sup>+</sup>CD80<sup>+</sup>CD86<sup>+</sup>/MHCII<sup>+</sup> dendritic cells) in tumor-draining lymph nodes (**g**,  $n = 6$  biologically independent samples) and T<sub>EM</sub> cells (CD45<sup>+</sup>CD3<sup>+</sup>CD4/8<sup>+</sup>CD62L<sup>-</sup>CD44<sup>+</sup>) in tumors (**h**,  $n = 6$  mice for saline, paclitaxel, and cisplatin;  $n = 5$  mice for doxorubicin and mtDSN-2) by flow cytometry. The data are presented as the mean  $\pm$  s.d. NS: not significant. Statistical analysis by log-rank test (**c**), one-way ANOVA with Turkey's (**f**, **g**) or Bonferroni's (**h**) multiple comparisons test. Source data are provided as a Source data file.

sustained for over 60 days (Fig. 6f, g), and the mice had a 100% survival rate (Fig. 6h). Immunofluorescence analysis revealed that mtDSN-2 treatment substantially promoted the recruitment of tumor-infiltrating CTLs, supporting the ICD-induced immune activation (Fig. 6i, j). We then rechallenged naive mice and mice cured from MC38 tumors by mtDSN-2 treatment by subcutaneously injecting them with MC38 cells. Interestingly, all cured mice but not naive mice persistently rejected tumor growth (Fig. 6k), suggesting that mtDSN treatment established systemic antitumor memory. Next, we performed flow cytometry profiling of peripheral blood monocytes (PBMCs) to examine the mechanism underlying immune memory response. Compared with vehicle control, mtDSN-2 markedly increased the CD4<sup>+</sup> and CD8<sup>+</sup> effector memory T-cell subsets (CD44<sup>+</sup>CD62L<sup>-</sup>, T<sub>EM</sub>) in cured mice, which may contribute to the long-term immune protection from recurring tumors (Fig. 6l and Supplementary Fig. 23). Additionally, spleens of mice treated with the combined therapy had higher proportions of both central memory T cells (CD62L<sup>+</sup>CD44<sup>+</sup>, T<sub>CM</sub>) and T<sub>EM</sub> than control after rechallenge, further supporting an evoked protective antitumor immune memory (Fig. 6m, n).

### mtDSN inflames the tumor microenvironment to enhance the ICB response

Despite the compelling clinical benefits of PD-1 blockade in various types of malignant cancer, patients eventually develop acquired resistance to this therapy after an initial response<sup>53</sup>. To address this, we established an anti-PD-1-resistant MC38 tumor model through the repeated administration of anti-PD-1 antibodies followed by serial implantation (Fig. 7a). Although PD-1 blockade exhibited significant tumor-suppressive activity in S0 (parental) tumors, serially implanted S3 tumors (termed MC38/R) were refractory to anti-PD-1 therapy (Fig. 7b). Immunostaining also revealed notable CTL exclusion (Fig. 7c, d) and macrophage polarization from antitumorogenic M1-like to protumorogenic M2-like in MC38/R tumors (Supplementary Fig. 24) compared with that in parental tumors, confirming the immune desertification of the TME and the acquired resistance established in this model. Subsequently, we assessed the effects of mtDSN-2 on proinflammatory remodeling of the TME and its synergism with anti-PD-1 therapy to increase immune response in this clinically relevant tumor model. The mtDSN-2 therapy caused significant MC38/R tumor regression and extended mouse survival (Fig. 7e–g). Notably, M2-to-M1-like repolarization of macrophages (Supplementary Fig. 24), abundance of intratumoral dendritic cells, and remarkable increase in tumor-infiltrating CTLs (Fig. 7h, i) supported the hypothesis that mtDSN-2 exerts immunomodulatory effects on tumors. More significantly, the combined mtDSN and anti-PD-1 regimen displayed a synergistic effect, with complete antitumor responses in six of nine mice and a striking increase in mice survival rate over 60 days (Fig. 7e–g).

Most patients with colorectal cancer have a mismatch repair-proficient or microsatellite-stable phenotype, and they rarely respond to anti-PD-1 monotherapy<sup>54</sup>. Therefore, we then evaluated the combination therapy in a nonhypermutated/microsatellite-stable CT26 tumor model<sup>55</sup>. As shown in Fig. 7j–l, CT26 subcutaneous tumors were

highly proliferative and aggressive, with only an 8-day median survival time. Additionally, the negligible antitumor efficacy of anti-PD-1 alone compared with saline control confirmed the primary resistance to anti-PD-1 therapy. By contrast, intratumoral mtDSN-2 exposure was effective and further synergized with PD-1 blockade, extending mouse survival and eradicating two out of the ten tumors. Immune profiling also showed that mtDSN-2 transformed immunologically silent TME into an inflamed one, as manifested by the enrichment in dendritic cells and increased recruitment of infiltrating CD8<sup>+</sup> T cells into CT26 tumors (Fig. 7m, n), consistent with the long-lasting antitumor response in the combination regimen. Overall, these preclinical results support that mtDSN-2-increased immunogenicity can potentiate the response to anti-PD-1 therapy, which may represent a promising strategy for treating ICB-refractory cancers.

### mtDSN transforms immunosuppressive and anti-PD-1-resistant tumors into “hot” tumors

Finally, to document how mtDSN therapy impacts the phenotype of tumor-infiltrating immune cells, we performed single-cell RNA sequencing (scRNA-seq) on the established anti-PD-1-resistant MC38 tumors with immune exclusion of CTLs. We projected discrete clusters of tumor-associated cell populations using *t*-distributed stochastic neighbor embedding (*t*-SNE) analysis (Fig. 8a) and annotated them based on the expression of canonical cell marker genes (Fig. 8b). Notably, mtDSN-2 treatment induced large shifts in the frequency and transcriptional state of numerous immune subsets, including a significant increase in the overall TILs (Fig. 8c). We then identified distinct T-cell states<sup>56</sup> and found that TILs from mtDSN-2-treated tumors were highly enriched in activated effector T-cell subsets, which were assigned primarily to exhausted (Tex) and effector memory (T<sub>EM</sub>) states (Fig. 8d and Supplementary Fig. 25). mtDSN-2 treatment decreased the proportion of regulatory T cells (Fig. 8e). Differentially expressed genes (DEGs) analysis revealed that the gene sets and pathways affected by mtDSN-2 were correlated with immune activation (Fig. 8f, g). Consistently, relative to vehicle control, TILs from mtDSN-2-treated tumors were featured by higher expression of *Irfng*, *Gzmk*, and *Gzmb*, suggesting an augmented effector function and cytolytic capacity (Fig. 8h). These findings provide compelling evidence that mtDSN-2 potentiates tumor cell immunogenicity, which unleashes CD8<sup>+</sup> T-cell-mediated effector functions. Cancer-associated fibroblasts (CAFs) in tumor tissues are closely associated with cancer progression and metastasis<sup>57</sup>. Indeed, mtDSN-2 notably reduced the population of CAFs in tumors (Fig. 8c). In particular, it significantly decreased the number and percentage of myofibroblastic CAFs (myCAFs)—which are associated with matrix-induced immune exclusion—as evidenced by the CAF landscape profiling (Supplementary Fig. 26). Further inspection of the DEGs showed that, compared with vehicle control, CAFs from mtDSN-2-treated tumors expressed remarkably lower levels of *Vegfa*, *Vegfb*, and *Vegfc*, associated with tumor angiogenesis; *Tgfb1*, *Tgfb2*, *Tgfb3*, and *Tgfb3*, associated with myCAF matrix production and function; while higher levels of cytokines such as *Il1a*, *Il1b*, *Ccl2*, and *Ccl5* (Fig. 8i), indicating the effects of therapy to induce inflamed TME.

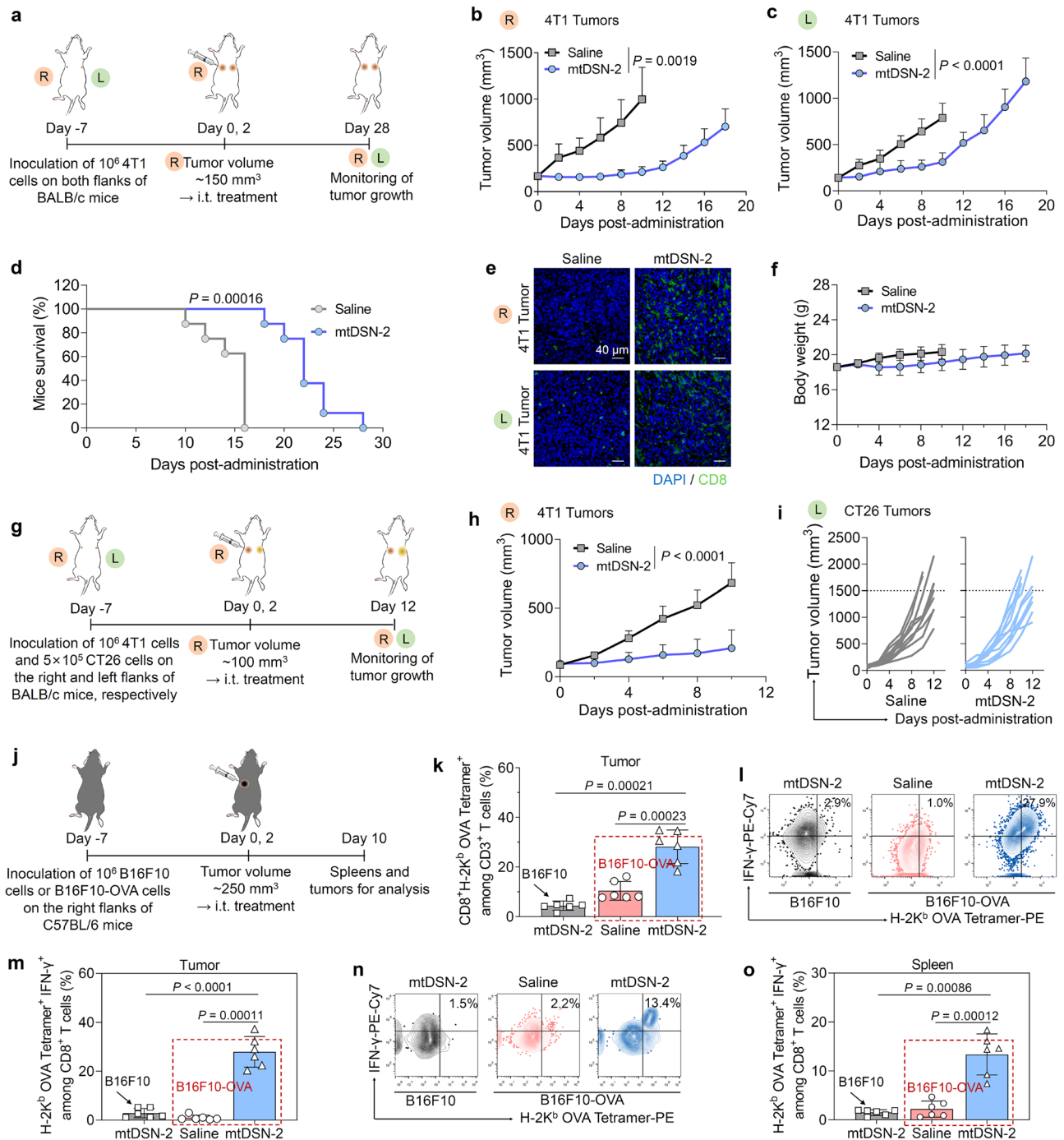


**Fig. 5 | Intratumoral mtDSN treatment induces abscopal effects with tumor-specific immunity.** **a** Schedule of the bilateral 4T1 tumor model for assessing the immune abscopal effect triggered by mtDSN-2 vaccination. i.t., intratumoral. Growth profiles of primary (**b**) and distant (**c**) tumors ( $n = 8$  mice/group). **d** Kaplan-Meier survival of 4T1 tumor-bearing BALB/c mice ( $n = 8$  mice/group). **e** Immunofluorescence staining of the tumor sections showed CD8<sup>+</sup> T-cell infiltration.  $n = 3$  mice/group. **f** Mouse body weights after each treatment ( $n = 8$  mice/group). **g** Schedule of bilateral heterologous tumor inoculation in BALB/c mice and treatment. Growth profiles of primary 4T1 tumors (**h**) and distant CT26 tumors (**i**)

( $n = 10$  mice/group). **j** Schedule of tumor antigen-specific T-cell activation analysis in mice with B16F10-OVA tumor. **k** H-2K<sup>b</sup>-restricted OVA<sub>257-264</sub>-specific CD8<sup>+</sup> T cells in tumors, as determined by flow cytometry analysis ( $n = 6$  mice/group). **l-o** Flow cytometry analysis and corresponding quantification of activated H-2K<sup>b</sup>-restricted OVA<sub>257-264</sub>-specific CD8<sup>+</sup> T cells in tumor (**l, m**) and spleen (**n, o**) tissues ( $n = 6$  mice/group). The data are presented as the mean  $\pm$  s.d. Statistical analysis by two-way ANOVA with Sidak's multiple comparisons test (**b, c, h**), log-rank test (**d**), or Student's *t* test (**k, m, o**). Source data are provided as a Source data file.

We also examined the impact of mtDSN-2 therapy on tumor-associated macrophages (TAM) and found that the treatment substantially reduced TAM infiltration (Fig. 8j). Further profiling unveiled that mtDSN-2 promoted the polarization of macrophages from the protumorigenic M2-like to antitumorigenic M1-like phenotype (Fig. 8j and Supplementary Fig. 27)<sup>58</sup>, manifested by decreased *Mrc1*

expression (Fig. 8k) and increased *Nos2* (Fig. 8l), *Il1a* (Fig. 8m), and *Il1b* (Fig. 8n) expression. GSEA identified several top hallmark pathways altered by mtDSN-2 treatment, among which the ROS production and proinflammatory pathways were upregulated in macrophages (Fig. 8o). Furthermore, mtDSN-2 treatment significantly increased the number of tumor-associated neutrophils (TANs) (Fig. 8p). Of note, the

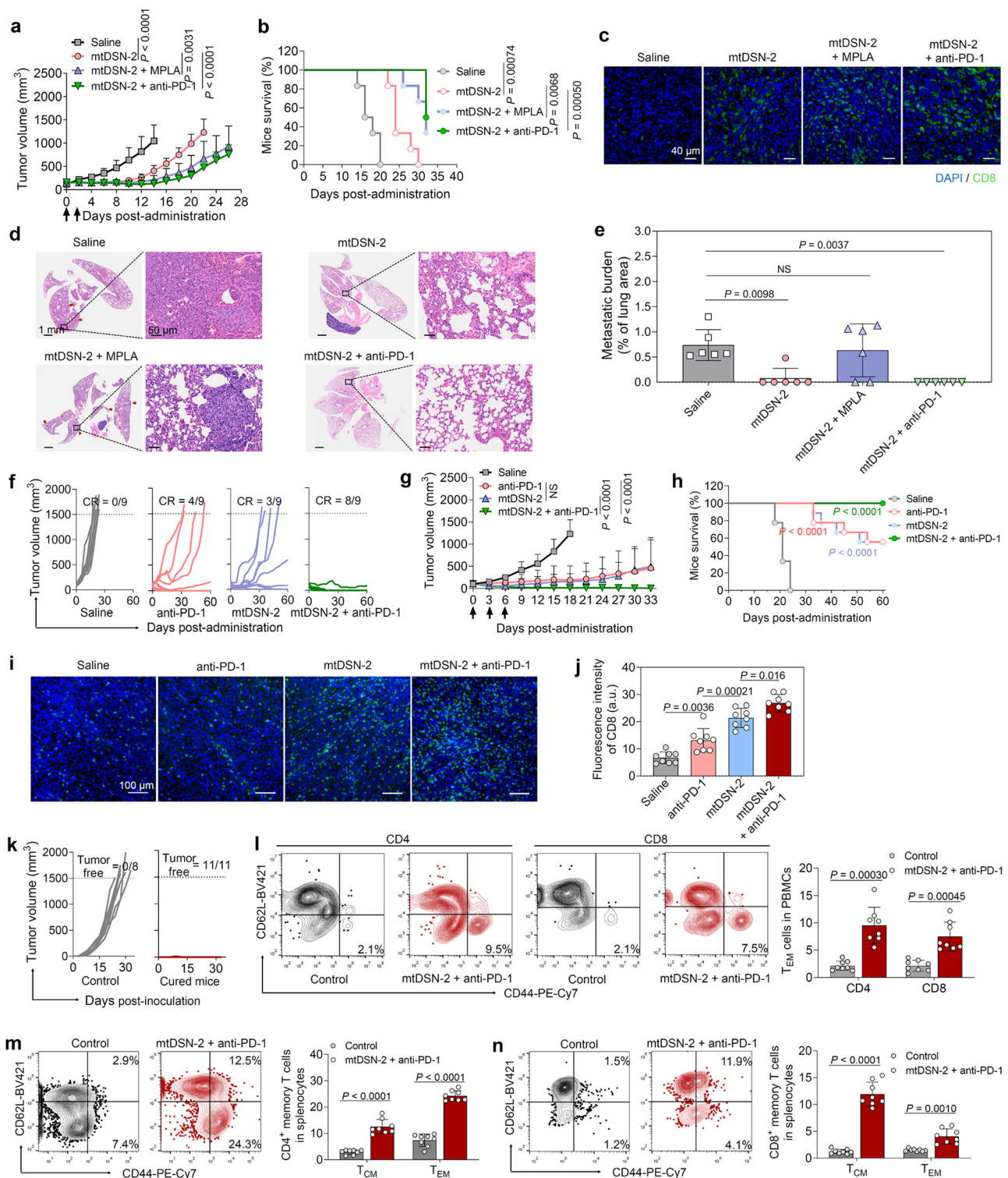


**Fig. 6 | mtDSN-2 synergizes with immunotherapies against solid tumors.** **a** Growth kinetics of 4T1 tumors after different treatments ( $n = 6$  mice/group). **b** Kaplan–Meier survival of 4T1 tumor-bearing BALB/c mice ( $n = 6$  mice/group). **c** Immunofluorescence staining of the tumor sections showed CD8<sup>+</sup> T-cell infiltration.  $n = 3$  mice/group. **d** H&E staining images of lung tissue sections. Red arrows indicate metastatic foci. The representative images are shown from six independent samples. **e** Quantification of the metastatic foci in lung tissues ( $n = 6$  mice/group). Mice were sacrificed and lungs were excised for analysis when tumor volume exceeded 1500 mm<sup>3</sup> or at the endpoint of the experiment. Individual MC38 tumor growth curves (**f**) and average tumor growth profiles (**g**) in each group ( $n = 9$  mice/group). **h**, Kaplan–Meier survival of MC38 tumor-bearing C57BL/6 mice ( $n = 9$  mice/group).  $P$  indicates the statistical significance relative to the saline-treated

group. Immunofluorescence staining of the tumors indicated CD8<sup>+</sup> T-cell infiltration (**i**) and the corresponding quantification (**j**), a.u., arbitrary units. Data of eight different views from 3 biologically independent samples. **k** Tumor growth curves after tumor rechallenge ( $n = 8$  for healthy control,  $n = 3$  for mtDSN-2, and  $n = 8$  for mtDSN-2 + anti-PD-1 cured mice). Flow cytometry plots and percentages of T<sub>EM</sub> (CD44<sup>+</sup>CD62L<sup>+</sup>) or T<sub>CM</sub> (CD44<sup>+</sup>CD62L<sup>+</sup>) cells in PBMCs (**l**) and spleens (**m**, **n**) from immunized mice on day 33 ( $n = 8$  mice/group). The data are presented as the mean  $\pm$  s.d. NS: not significant. Statistical analysis by two-way ANOVA with Turkey's multiple comparisons test (**a**, **g**), log-rank test (**b**, **h**), one-way ANOVA with Turkey's multiple comparisons test (**e**, **j**), or Student's *t* test (**l**–**n**). Source data are provided as a Source data file.

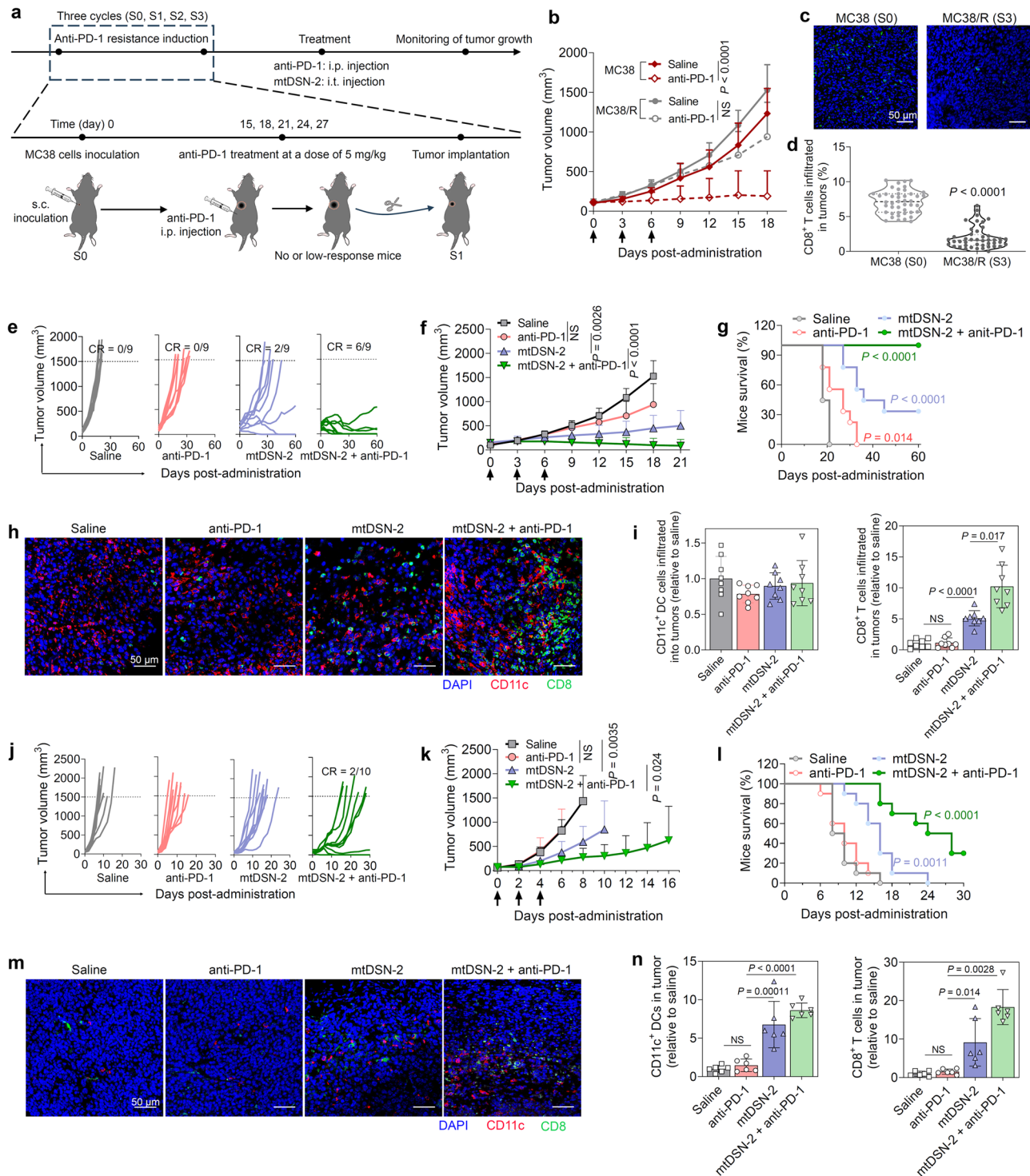
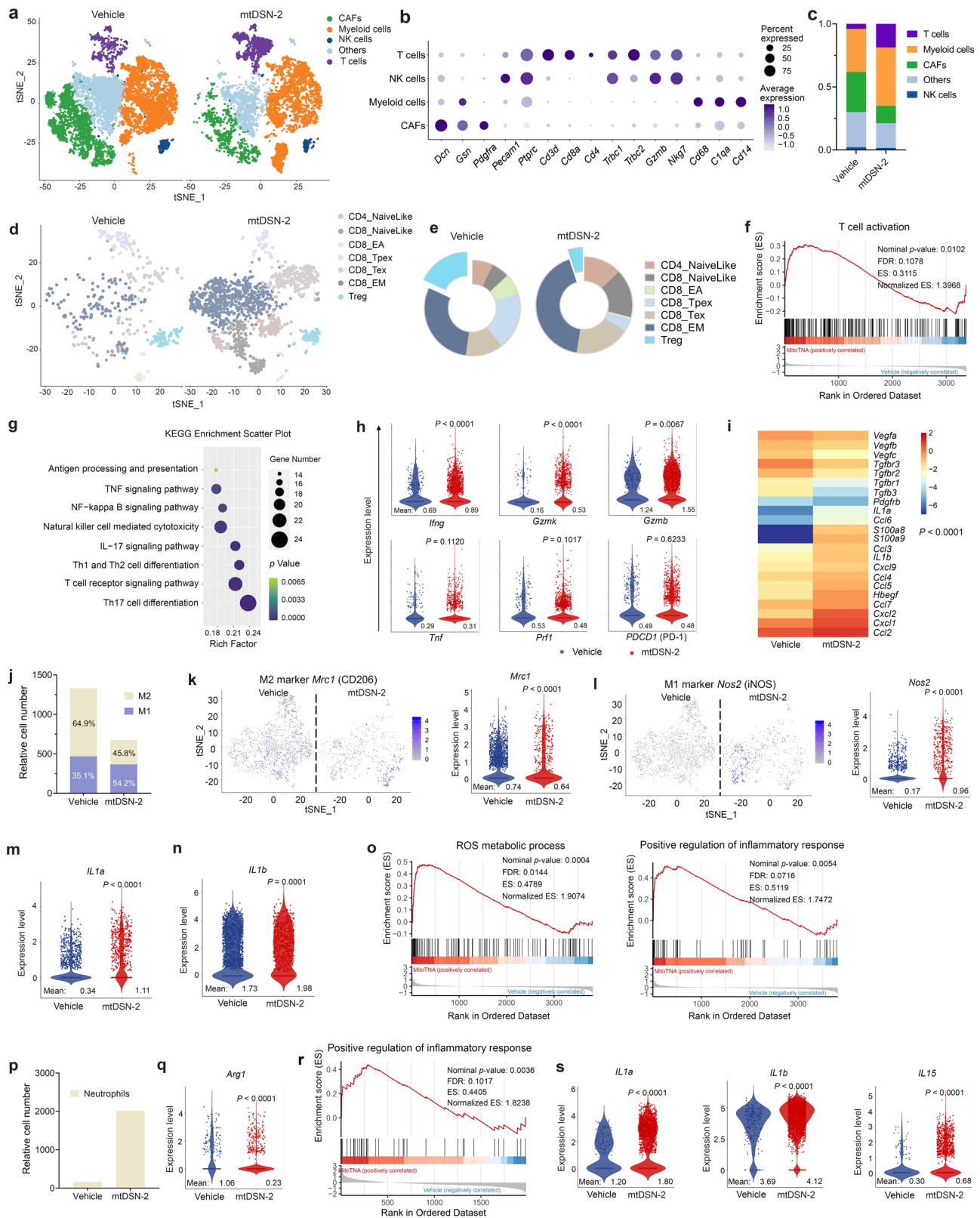


**Fig. 7 | mtDSN-2 inflames the tumor microenvironment to enhance ICB response.** **a** Schedule for inducing resistance to PD-1 blockade in MC38 tumors to assess the immune synergy of mtDSN-2 to ICB. i.p., intraperitoneal, i.t., intratumoral, s.c., subcutaneous. **b** Tumor growth kinetics of MC38 and MC38 anti-PD-1-resistant tumors (MC38/R) in response to PD-1 blockade ( $n = 9$  mice/group). Immunofluorescence staining (**c**) and quantitative analysis (**d**) of CD8<sup>+</sup> T-cell infiltration in S0 and S3 tumors. Statistics from four independent tumors. Individual MC38/R tumor growth curves (**e**) and average tumor growth profiles (**f**) in each group ( $n = 9$  mice/group). **g** Kaplan–Meier survival of MC38/R tumor-bearing C57BL/6 mice ( $n = 9$  mice/group).  $P$  indicates the statistical significance relative to the saline-treated group. Immunofluorescence staining (**h**) and quantitative analysis (**i**) of CD11c<sup>+</sup> dendritic cell and CD8<sup>+</sup> T-cell infiltration in tumors. Data of eight

different views from 3 biologically independent samples. Individual CT26 tumor growth curves (**j**) and average tumor growth curves (**k**) in BALB/c mice ( $n = 10$  mice/group). **l** Kaplan–Meier survival of CT26 tumor-bearing BALB/c mice ( $n = 10$  mice/group).  $P$  indicates the statistical significance relative to the saline-treated group. Immunofluorescence staining (**m**) and quantitative analysis (**n**) of CD11c<sup>+</sup> dendritic cell and CD8<sup>+</sup> T-cell infiltration in CT26 tumors. Data of six different views from three biologically independent samples. The data are presented as the mean  $\pm$  s.d. NS: not significant. Statistical analysis by two-way ANOVA with Turkey’s multiple comparisons test (**b, f, k**), Student’s  $t$  test (**d**), log-rank test (**g, l**), Brown-Forsythe and Welch ANOVA with Dunnett’s T3 multiple comparisons test (**i**), or one-way ANOVA with Turkey’s multiple comparisons test (**n**). Source data are provided as a Source data file.



expression of arginase-1 (*Arg1*), a pivotal enzyme contributing to tumor immune evasion<sup>59</sup>, was substantially reduced in neutrophil clusters following mtDSN-2 therapy (Fig. 8q). The enrichment analysis revealed that mtDSN-2 stimulated the specific pathways of TANs related to proinflammatory immune activation (Fig. 8r and Supplementary Fig. 38), with *IL1a*, *IL1b*, and *IL15* particularly upregulated (Fig. 8s). Additionally, mtDSN-2 upregulated *CD274* (PD-L1) expression across tumor and immune cells (Supplementary Fig. 29), further

supporting the rationale of improving immunotherapy efficacy with ICB inhibitors.

## Discussion

Developing therapeutic strategies able to promote an immunogenic tumor phenotype and increase response to ICB therapy with minimal systemic inflammation and toxicity remains a central challenge for effective immunotherapy. Recent evidence has highlighted that

**Fig. 8 | mtDSN-2 reprograms immunosuppressive TME in MC38 tumors that are refractory to anti-PD-1 immunotherapy.** **a** t-SNE plots of tumor scRNA-seq data ( $n = 3$  samples were pooled to control for biological variability). CAFs, cancer-associated fibroblasts. **b** Bubble plot outlines the expression of canonical lineage cell markers used for cell cluster annotation. The percentage expressed in each subset is indicated by the size of the dots, and average expression intensity is indicated by color. **c** Stacked bar plots show the percentages of the different cell clusters in the two treatment conditions (Vehicle and mtDSN-2) by scRNA-seq. **d** T cells-only t-SNE projection shows emergent sub-clusters. Supervised T-cell state classification confirms different functional T-cell subsets: naive-like, early activated (EA), progenitor exhausted (T<sub>pe</sub>), exhausted (T<sub>ex</sub>), effector memory (EM) and regulatory T cells (T<sub>reg</sub>). **e** Donut chart shows the proportion of T-cell subsets in two treatment conditions. **f** Gene set enrichment analysis (GSEA) of DEGs showing gene set enrichment associated with cell activation of T cells following mtDSN-2 treatment. FDR, false discovery rate, ES, enrichment score. **g** Kyoto encyclopedia of genes and genomes (KEGG) pathway enrichment analysis of DEGs showing

pathways associated with antitumor response of T cells. **h** Violin plots represent the expression of activation and cytotoxicity markers in the T-cell subset. **i** Heat map of representative DEGs in CAFs. **j** Stacked bar plot showing the proportion of M1 and M2-like clusters in macrophages. **k**, **l** t-SNE projection of macrophages reveals *Mrc1* (CD206) and *Nos2* (iNOS) single-cell transcripts that are clustered in the high-dimensional space in two treatment conditions and then quantified with violin plot. **m**, **n** Violin plots represent the expression of *IL1a* and *IL1b* in the macrophage subset. **o** GSEA of DEGs showing gene set enrichment associated with ROS production and proinflammation in macrophages following mtDSN-2 treatment. **p** Increased neutrophils recruitment following mtDSN-2 treatment. **q** Violin plot representing the expression of the *Arg1* gene in the neutrophil subset. **r** GSEA of DEGs showing gene set enrichment associated with proinflammation in neutrophils following mtDSN-2 treatment. **s** Violin plots representing the expression of indicated genes in the neutrophil subset. Statistical analysis by permutation test (**f**, **o** and **r**) and Wilcoxon rank sum test (**h**, **k–n**, **q** and **s**). Source data are provided as a Source data file.

mitochondria are a critical hub for boosting the antitumor immune response via the inflammation of immune-desert tumors<sup>16</sup>. For example, mitochondrial DNA released upon disruption of mitochondria, besides acting as a DAMP and activating the NLRP3 inflammasome and TLR9 to induce an inflammatory response may also activate the stimulator of interferon genes signaling pathway<sup>60,61</sup>. In addition, mitochondrial biogenesis, dynamics, and ROS production regulate the function of some subsets of tumor-infiltrating immune cells<sup>62,63</sup> and also have roles in T-cell activation<sup>64,65</sup>. All these findings indicate that mitochondria are a potential target for enhancing tumor immunogenicity or to synergize with current immunotherapies. Here, we conceived a small-molecule-based dynamic nanosystem to target this cellular organelle, whose cytotoxic mechanism differs from conventional chemotherapy. Very interestingly, we observed aggregation-induced cytotoxicity, and the dissociation of the nanoassemblies attenuated this activity, hopefully indicating that these nanoassemblies could become low-toxicity and traceless cancer therapy. Indeed, mtDSN-2 was less cytotoxic on hepatocytes than on cancer cells observed in in vitro assays (Supplementary Fig. 30a). Intratumoral administration of mtDSN-2 did not impart any side effects on major healthy tissues (Supplementary Fig. 30b) while inducing extensive apoptotic cell death in tumors (Supplementary Fig. 30c), suggesting its favorable safety profile for the preclinical use. Morphological observation by TEM and SEM suggested that these nanoassemblies act as nanobombs directly disrupting the mitochondrial membrane and causing lethal damage on mitochondria. Although further studies are warranted to elucidate the underlying molecular mechanisms, we hypothesize that incorporating massive amounts of exogenous polyunsaturated fatty acids into mitochondrial membrane phospholipids disrupts the mitochondrial stability and permeability, leading to deformed membrane structure<sup>66</sup>.

Mechanistic experiments revealed that the mtDSN platform substantially impeded mitochondrial biogenesis in tumor cells. The overwhelming mitochondrial stress, induced by mtDSN-2, also perturbed ER homeostasis through excessive ROS production and potential imbalance in substance exchanges, leading to irreversible ER stress<sup>41</sup>. This pronounced ER stress facilitated the activation of subsequent cellular death programs through both paraptosis and apoptosis pathways. Additionally, we observed that stressed and injured tumor cells emitted various DAMPs, including surface-exposed CRT, passively released HMGB1, and secreted ATP. These danger signals stimulated immunological responses by eliciting the ICD cascade and converted immunologically silent tumors into inflamed ones. So far, various ICD inducers (including chemotherapeutic agents, such as doxorubicin and oxaliplatin) have been reported to incite antitumor immunity<sup>12,45,46</sup>. In addition, cancer cells treated ex vivo with these agents and then implanted subcutaneously function as a vaccine, yielding potent anticancer immunity<sup>67</sup>. Compared with chemotherapy-

based bona fide ICD inducers (e.g., doxorubicin), mtDSN-2 induced notable ICD efficiency but demonstrated fewer side effects in vivo (published elsewhere), presumably due to its aggregation-dependent cytotoxic potential. After performing their antitumor activity, these noncovalent assemblies should dissociate into nontoxic small molecules, thereby contributing to the favorable safety profile of this platform in animals.

mtDSN treatment converted injured cancer cells into either a prophylactic vaccination regimen or therapeutic vaccine and also triggered a localized inflammatory antitumor immune cascade in multiple syngeneic models, including those refractory to PD-1 blockade. Last, a high-dimensional interrogation of tumors with scRNA-seq revealed that this mtDSN platform profoundly remodeled the TME, enlisting activated effector T-cell populations executing a cell-killing activity highly hinged on IFN- $\gamma$  and granzyme expression, and reducing TAM infiltration while clearly shifting the macrophage phenotype from M2-like to the proinflammatory M1-like. TANs can exert dual functions; they either promote tumor progression by driving angiogenesis, metastasis, and immunosuppression, or mediate antitumor responses by directly killing cancer cells<sup>59</sup>. Unexpectedly, mtDSN exposure increased neutrophils recruitment while transforming neutrophils into antitumor phenotype on the basis of TANs plasticity<sup>68</sup>. Consistently, the expression of the proinflammatory chemokine *CXCL2*, which is responsible for neutrophil recruitment in mice<sup>69</sup>, was widely upregulated in all cells (Supplementary Fig. 31). Moreover, the profound *S100A8/A9* overexpression throughout the tumors might also account for neutrophil accumulation and proinflammatory cytokine secretion, whose high levels are characteristic for leukocyte recruitment and inflammatory conditions (Supplementary Fig. 32)<sup>70</sup>. Accumulating evidence showed that exposure to proinflammatory cytokines, such as IFN- $\gamma$ , TNF- $\alpha$ , and interleukins, could trigger the adaptive expression of PD-L1<sup>71</sup>, thereby promoting the immune escape of tumor cells. Indeed, we found that mtDSN-treated tumors featured considerable PD-L1 upregulation and tested the feasibility of combining mtDSN with ICB therapy in animal models.

In summary, we have described the example of nontherapeutic small molecular ICD nanoinducer and identified its mechanism of mitochondria/ER-associated ICD induction that substantially potentiated tumor immunogenicity and unleashed the full potential of T-cell based therapy. As a traceless therapy, this mitochondria-targeting and rewiring platform has established its high safety profile and warrants further investigations for stimulating anticancer immune responses.

## Methods

### Ethical statement

We performed animal experiments in accordance with the National Institute Guide for the Care and Use of Laboratory Animals. The experimental protocols were approved by the Ethics Committee of the

First Affiliated Hospital, Zhejiang University School of Medicine. All studies comply with relevant ethical regulations.

## Materials

Diverse fatty acids were purchased from Sigma Aldrich (USA). 3-(aminopropyl)triphenylphosphonium (TPP) bromide was purchased from Macklin Biochemical Co., Ltd. (Shanghai, China). Paclitaxel, doxorubicin and cisplatin were purchased from Tokyo Chemical Industry (Shanghai, China). Cell death inhibitors were purchased from MedChemExpress (USA). Recombinant murine granulocyte/macrophage colony-stimulating factor (GM-CSF) and mIL4 were purchased from PeproTech Inc. (USA). Monophosphoryl lipid A (MPLA) was purchased from InvivoGen (Cat #vac-mpls, France). Cell culture reagents were purchased from Biological Industries (Israel). All of other solvents and compounds were purchased from J&K Chemical (Shanghai, China) and used without further purification.

## Cell lines

The mouse melanoma cell lines, B16F10 and B16F10-OVA, mouse mammary carcinoma cell line, 4T1, mouse colorectal cancer cell lines, MC38 and CT26, human cervical cancer cell line, HeLa, human non-small-cell lung cancer cell line, A549, human ovarian cancer cell line, A2780, and mouse hepatocytes, AML12, were purchased from the cell bank of the Chinese Academy of Sciences (Shanghai, China), Crisprbio (Beijing, China), and Bowers Type Culture Collection (Beijing, China). Immortalized human hepatocyte cell line, HepLi5, was a gift from Professor Li Lanjuan's team at the State Key Laboratory for Diagnosis and Treatment of Infectious Diseases, First Affiliated Hospital, School of Medicine, Zhejiang University. Drug-resistant cell lines HeLa/R, A549/R and A2780/R were established following method of increasing cisplatin concentration. Cancer cells were maintained in Roswell Park Memorial Institute 1640 or Dulbecco's modified Eagle's medium (Biological Industries) supplemented with 10% (v/v) fetal bovine serum (FBS) (Biological Industries), 100 U ml<sup>-1</sup> penicillin (Biological Industries) and 100 µg ml<sup>-1</sup> streptomycin (Biological Industries) and cultured in a humid atmosphere containing 5% CO<sub>2</sub> at 37 °C. For siRNA mediated silencing of Sec61b and caspase 3, 4T1 cells were transfected with 100 nM Sec61b siRNA, caspase 3 siRNA or untargeted Mock control (GenePharma, China) for 48–72 h prior to assay.

## Mice

BALB/c mice (female) and C57BL/6 mice (male) were purchased from the Laboratory Animal Center of Hangzhou Medical College (Hangzhou, China). Six- to eight-week-old mice were used throughout the *in vivo* studies. All mice were kept in specific pathogen-free conditions at 23–26 °C, 40–60% humidity and under a 12/12 h light/dark cycle. The mice were euthanized via CO<sub>2</sub> inhalation when tumor volume exceeded 1500 mm<sup>3</sup> in accordance with the animal ethics guidelines of our institute and animal welfare regulations (<2000 mm<sup>3</sup>).

## Antibodies

The anti-PD-1 antibody used *in vivo* was purchased from Bio X Cell (29F.1A12<sup>™</sup>, #BPO273, lot 883023J1). The primary antibodies used for immunostaining were against CD45 (30-F11, Biolegend, #103112, lot B353749, 80×), CD11c (N418, Biolegend, #117318, lot B346713, 80×), CD80 (16-10A1, Biolegend, #104706, lot B342942, 80×), CD86 (GL-1, Biolegend, #105028, lot B317511, 80×), MHC II (M5/114.15.2, Biolegend, #107632, lot B360796, 80×), CD3 (17A2, Biolegend, #100228, lot B343124, 80×), CD4 (GK1.5, Biolegend, #100408, lot B334826, 80×), CD8a (53-6.7, BD Biosciences, #750024, lot 2214082, 40×; KT15, Thermo Fisher Scientific, #MA5-16759), CD44 (IM7, BD Biosciences, #560569, lot 1221629, 40×), CD62L (MEL-14, BD Biosciences, #562910, lot 1293954, 40×), intracellular IFN-γ (XMGL2, Biolegend, #505826, lot B367890, 80×), and CD16/32 (93, Biolegend, #101302, lot B361754,

80×). The stained cells were analyzed on a CytoFLEX LX flow cytometer (Beckman), using the FlowJo or CytExpert software packages. Multi-color flow cytometry was used with appropriate compensation. The primary antibodies used for immunoblotting and immunofluorescence were against Drp1 (EPR19274, Abcam, #ab184247, lot GR3369203-11, 1000×), caspase 9 (C9, Cell Signaling Technology, #9508, lot 7, 1000×), cleaved caspase 9 (D2D4, Cell Signaling Technology, #7237, lot 3, 1000×), caspase 3 (Cell Signaling Technology, #9662, lot 19, 1000×), cleaved caspase 3 (5A1E, Cell Signaling Technology, #9664, lot 22, 1000×), PARP (Cell Signaling Technology, #9542, lot 15, 1000×), Bcl-2 (D17C4, Cell Signaling Technology, #3498, lot 6, 1000×), Bim (Abclonal, #A0295, lot 3100170101, 1000×), Bax (E63, Abcam, #ab32503, 1000×), cytochrome c (6H2.B4, Beyotime, #AC908, lot 091223240402, 500×), TOM20 (ARC5002-01, Abclonal, #A19403, lot 3600001090, 100×), calreticulin (D3E6, Cell Signaling Technology, #12238, lot 5, 500×), HMGB1 (Cell Signaling Technology, #3935, lot 4, 50×), PERK (EPR19876-294, Abcam, #ab229912, 1000×), p-PERK (16F8, Cell Signaling Technology, #3179, lot 21, 300×), eIF2α (D7D3, Cell Signaling Technology, #5324, lot 9, 1000×), p-eIF2α (D9G8, Cell Signaling Technology, #3398, lot 8, 1000×), ATF4 (Abclonal, #A21500, lot 5500038538, 1000×), CHOP (L63F7, Cell Signaling Technology, #2895, lot 15, 1000×), HRI (Proteintech, #20499-1-AP, 1000×), Ubiquitin (ARC50024, Abclonal, #A19686, lot 6100005203, 1000×), Sec61b (Abclonal, #A15788, lot 0161690101, 1000×), 4-HHE/HNE (6F10, Novus Biologicals, #NBP2-59352, 50×), CD11c (DIV9Y, Cell Signaling Technology, #97585, lot 6, 300×), F4/80 (D2S9R, Cell Signaling Technology, #70076, lot 9, 300×), CD86 (E5W6H, Cell Signaling Technology, #19589, lot 5, 300×), CD206 (E6T5J, Cell Signaling Technology, #24595, lot 3, 300×), β actin (8H10D10, Cell Signaling Technology, #3700, lot 21, 1000×), VDACL/2 (Proteintech, #10866-1-AP, 1000×), NaK ATPase (EP1845Y, Abcam, #ab76020, 100000×), isotype control (E7Q5L, Cell Signaling Technology, #53484, lot 4; DAIE, Cell Signaling Technology, #3900, lot 52). The secondary antibodies used for immunostaining were horse anti-mouse IgG, HRP linked (Cell Signaling Technology, #7076P2, lot 36, 2000×), goat anti-rabbit IgG, HRP linked (Cell Signaling Technology, #7074P2, lot 33, 2000×), donkey anti-rabbit IgG Alexa Fluor<sup>™</sup> 555 (H + L; Thermo Fisher Scientific, #A31572, 500×), donkey anti-rabbit IgG Alexa Fluor<sup>™</sup> 488 (H + L; Thermo Fisher Scientific, #A21206, 1000×), goat anti-mouse IgG Alexa Fluor<sup>™</sup> 488 (H + L; Thermo Fisher Scientific, #A11001, 1000×).

## Preparation of dynamic supramolecular nanoassemblies

Fatty acid-TPP conjugates were dissolved in DMSO and then slowly injected into deionized water under ultrasonication to prepare the self-assembled nanoparticles. The volume ratio of DMSO to deionized water was fixed at 5%. Prior to further use, the as-prepared nanoassemblies were dialyzed against deionized water to remove the organic solvent. The drug concentration was determined via high-performance liquid chromatography analysis at a wavelength of 220 nm using a C8 reverse-phase column (5 µm, 250 mm × 4.6 mm, YMC Co., Ltd., Kyoto, Japan). A gradient of 50–100% acetonitrile in water within 25 min was adopted as the mobile phase at a flow rate of 1 mL/min.

## Cytotoxicity study using MTT assay

Tumor cells were seeded in 96-well plates and incubated at 37 °C overnight. Then, the cells were incubated with different agents at serially diluted concentrations for 48 or 72 h. At the end of the incubation period, 30 µl of 3-[4,5-dimethylthiazol-2-yl]-3,5-diphenyl tetrazolium bromide (MTT) solution (5 mg ml<sup>-1</sup>) was added and incubated at 37 °C for 4 h. Afterwards, the MTT solution was replaced with 100 µl dimethyl sulfoxide to dissolve the purple MTT-formazan crystals. The absorbance in each individual well was then measured at 490 nm using a microplate reader (Multiskan FC, Thermo Scientific). The viability of untreated cells was defined as 100%. IC<sub>50</sub> was calculated with the following formula:  $Y = 100/[1 + ([X/IC_{50}]^n)^{-1}]$ . Herein, *Y* represents cell

viability,  $X$  is the compound concentration, and the initial value of  $P$  is 0.05.

### Cellular endocytosis pathways

To verify energy-dependent endocytosis, cells were treated with Cy5.5-labeled mtDSN at 37 °C or 4 °C for 2 h before flow cytometry analysis. To determine the possible endocytosis pathway, HeLa/R cells were pre-treated with various inhibitors for 0.5 h to block specific endocytosis. Specifically, cytochalasin D (40 μM) was used to block macropinocytosis, filipin (5 μg/mL) was used to block caveolin-mediated endocytosis, and chlorpromazine (10 μg/mL) was used to block clathrin-mediated endocytosis. Then, Cy5.5-labeled mtDSN was added to a final Cy5.5 concentration of 0.2 μM and continued to incubate for 4 h. Finally, cells were collected, washed with cold phosphate-buffered saline (PBS), and submitted to flow cytometry analysis.

### Intracellular distribution

Cells were incubated with Cy5.5-labeled mtDSN for 3 h and 6 h, respectively. Following washed with PBS three times, cells were subsequently stained with LysoTracker Red DND-99 and Hoechst 33342 at 37 °C for 30 min. After brief wash, cells were observed under confocal laser fluorescence microscopy (CLSM, Olympus IX83-FV3000, Japan). Z-stack images were further taken for 3D remodeling (Imaris software) by moving the focal plane of the microscope incrementally through the cells.

### Mitochondria isolation

We isolated mitochondria using a cell mitochondria isolation kit (Solarbio, China) according to the manufacturer's protocol. Tumor cells were collected in precooled lysis buffer supplemented with a protease inhibitor cocktail (MedChem Express) and adequately homogenized. Then, the suspensions were obtained by centrifugation at 1000 *g* for 5 min followed by further precipitating mitochondria at 12,000 *g* for 10 min. Pelleted mitochondria were further purified by mito-wash buffer (supplied in kit) and resuspended in storage buffer for further use.

### Electron microscopy

For TEM analysis, solutions of mtDSNs were dipped into a carbon-coated 300-mesh copper grid for 3 min. Then, the solution was removed with filter paper. Two wt% aqueous uranyl acetate solution was used to stain the samples before observation. Tumor cells were treated with different agents (5 μM) and fixed with 2.5% glutaraldehyde overnight at 4 °C. After further fixation in 1% osmium tetroxide for 1 h and 2% uranyl acetate for 0.5 h, we dehydrated the cells in a graded solvent series (50, 70, 90, and 100% ethanol for 15 min each time and 100% acetone twice for 20 min). Samples were further permeated, and underwent fixation in embedding medium. Ultratome V (LKB) ultramicrotome was used to prepare Ultrathin sections (60–70 nm). Finally, we counterstained the sections using uranyl acetate and lead citrate. The images were obtained using TEM (Talos L120C, Thermo) at an acceleration voltage of 120 kV.

For SEM characterization, mitochondria isolated from tumor cells were incubated at 4 °C for 30 min with or without 0.5 μM mtDSN-2, then fixed with 2.5% glutaraldehyde at room temperature for 2 h, followed by overnight at 4 °C. Subsequently, the cells were washed three times with PBS, fixed with 1% osmium tetroxide, dehydrated through a graded series of ethanol concentrations (30, 50, 70, 80, 90, and 95% for 15 min each time and 100% for 20 min twice). After vacuum drying, the samples were coated with gold/palladium and analyzed by SEM using a Nova Nano 450 (Nova Nano 450, Thermo).

### mtDSN accumulation in mitochondria

Cy5.5 conjugated linoleic acid (Cy5.5-LA) was synthesized as described previously<sup>24</sup> and self-assembled to obtain nDSN as a control. mtDSN

was labeled with fluorescent dye Cy5.5 by co-assembly with Cy5.5-LA. Cells were incubated with nDSN or Cy5.5-labeled mtDSN at a final Cy5.5 concentration of 0.2 μM. For CLSM analysis, MitoTracker Green (Beyotime, China) was added to stain the mitochondria. For flow cytometry analysis, mitochondria were isolated and subjected to flow cytometer (CytoFLEX LX, Beckman) to quantify the fluorescence intensity in the mitochondrial fractions. Untreated cells were included as a negative control.

### Annexin V-FITC/propidium iodide (PI) dual staining

The cell apoptotic rate was detected using an Annexin V-FITC/PI kit (Dojindo, Japan) according to the manufacturer's instructions. Tumor cells were incubated with fresh medium containing different drugs for 48 h. Collected cells were stained with Annexin V-FITC and PI for 15 min and then subjected to flow cytometry (Cytoflex, Beckman Coulter) analysis.

### Immunoblotting

Tumor cells for western blot analysis were seeded and treated as described in the figure legends. Cells were collected and lysed in RIPA lysis buffer supplemented with a protease and phosphatase inhibitor cocktail (MedChem Express) on ice. Proteins were extracted and the concentration was determined following a standard protocol. An equivalent amount of protein was separated by sodium dodecyl sulfate-polyacrylamide gel electrophoresis (SDS-PAGE, GenScript), transferred onto polyvinylidene difluoride membranes, and then detected with the corresponding antibodies. The phos-tag™ SDS-PAGE (Wako Chemicals, Japan) were used to monitor protein phosphorylation according to the manufacturer's instructions.

### Quantitative RT-PCR (qPCR)

Total RNA was extracted from 4T1 cells via TRIzol (Life Technologies). Reverse transcription was conducted using the HiScript III All-in-one RT SuperMix Perfect for qPCR kit (Vazyme, China). qPCR reactions were performed with ChamQ Universal SYBR qPCR Master Mix on a real-time quantitative PCR detecting system (LightCycler 480, Roche) using the following oligonucleotide primers: caspase 3-Fwd: 5'-TGGTGATGAAGGGGTCATTATG-3', caspase 3-Rev: 5'-TTCGGCTTCCAGTCAGACTC-3', Sec61b-Fwd: 5'-CCCAGTGCTGGTGATGAGTC-3', and Sec61b-Rev: 5'-GCCCAATCTATGATCGCGTG-3'.

### Measurement of total mitochondrial proteins

After cells were treated with agents (5 μM) for 48 h, mitochondria were isolated and lysed with RIPA lysis buffer (MedChem Express). The concentration of total mitochondrial proteins was quantified using a MicroBCA assay kit (Thermo Scientific) following the manufacturer's protocol.

### Citrate synthase activity

Cells were treated with various agents at a concentration of 5 μM for 48 h. Subsequently, mitochondria were isolated from the cells to measure citrate synthase activity using a citrate synthase activity assay kit (Solarbio, China) following the manufacturer's protocol.

### Reactive oxygen species (ROS)

Tumor cells were treated with agents (5 μM) for 24 h. For total intracellular ROS detection, cells were stained with 10 μM DCFH-DA (Solarbio, China) and Hoechst 33342 (Beyotime, China) at 37 °C for 20 min and 10 min, respectively. Then, cells were washed with fetal bovine serum-free medium three times to remove the residual probe and then subjected to microscopy analysis. To measure mitochondrial ROS generation, cells were stained with 500 nM MitoSOX™ red mitochondrial superoxide indicators (Invitrogen) for 30 min at 37 °C before subjected to flow cytometry and CLSM analysis.



### Lipid peroxidation

Tumor cells were treated with 5  $\mu\text{M}$  agents for 36 h. For the malondialdehyde (MDA) measurement, MDA concentration in cellular extracts was determined with an MDA detection kit (Solarbio, China) according to the manufacturer's instructions. To quantify intracellular 4-Hydroxynonenal (4-HNE), cells were fixed with 90% methanol at 4 °C for 10 min followed by permeabilization with 0.5% Triton X-100 in PBS for 10 min. After blocking with 3% bovine serum albumin, cells were stained with anti-4-HNE antibody (1:50) or mouse (E7Q5L) mAb IgG2b isotype control (1:125, Cell Signaling Technology, cat. no. 53484) at 4 °C for 30 min. Cells were further stained with goat anti-mouse IgG Alexa Fluor™ 488 (1:200) for 30 min at room temperature before the flow cytometry analysis.

### ER mass enlargement

Cells were treated with various agents at a concentration of 5  $\mu\text{M}$  for 36 h. Then, cells were stained with 500 nM of ER tracker green (Beyotime, China) at 37 °C for 30 min, followed by flow cytometry analysis and CLSM observation.

### Immunofluorescence staining

Tumor cells were incubated in medium containing different agents (5  $\mu\text{M}$ ) for 12–36 h. After washing with PBS, cells were fixed with 4% paraformaldehyde for 30 min and permeabilized with 0.5% Triton X-100 in PBS for 10 min. The samples were further blocked with 3% bovine serum albumin for 1 h at room temperature. Then, cells were successively incubated with corresponding antibodies and a secondary antibody coupled with Alexa Fluor 488. DAPI was used to stain the nuclei. Rhodamine Phalloidin was used to stain F-actin. Dil (10  $\mu\text{M}$ ) was added to stain the cell membrane for 30 min followed by washing with PBS for 5 min three times at 37 °C. For Drp1 redistribution analysis, cells were stained with MitoTracker Red CMXRos (Beyotime, China) before paraformaldehyde fixation. Cells were observed using CLSM (OLYMPUS IX83-FV3000).

### ICD detection

Tumor cells were incubated in medium containing different agents (5  $\mu\text{M}$ ) for 36 h. For flow cytometry analysis of cell surface exposure of CRT, tumor cells were carefully harvested using cell scrapers, washed twice with cold PBS, fixed in 0.25% paraformaldehyde for 5 min, and blocked with 3% fetal bovine serum for 15 min. Then, cells were incubated with anti-CRT antibody (1:500) or rabbit (DA1E) mAb IgG XP® isotype control (1:4926, Cell Signaling Technology, cat. no. 3900) at 4 °C for 30 min. After washed with PBS for three times, cells reacted with donkey anti-rabbit IgG Alexa Fluor™ 488 (1:200) at 4 °C for 30 min. The cells were then stained with PI (BD Biosciences) before flow cytometry examination. The cells were gated on PI-negative cells. For the immunoblotting analysis of cell surface CRT, purification of plasma membrane proteins was achieved using a minute™ plasma membrane protein isolation and cell fractionation kit (Invent Biotechnologies, SM-005). Anti-NaK ATPase was used to control equal loading. Intracellular HMGB1 distribution was tested using immunofluorescence analysis. Extracellular HMGB1 release into cell culture media was measured using ELISA kit (Solarbio, SEKH-0409 and SEKM-0145) according to the manufacturer's instructions. The intracellular and extracellular ATP levels were measured by an ATP assay kit (Beyotime, S0027). Cellular protein was quantified for normalization. The luminometric measurement was performed on a Varioskan Flash (Thermo).

### In vitro BMDC maturation

BMDCs were prepared according to the reported protocol. In brief, bone marrow was flushed from isolated femurs of C57BL/6j mice using PBS. After RBC lysis, bone marrow cells were seeded in petri dishes and cultured with dendritic cell medium (Dulbecco's Modified Eagle

Medium supplemented with 10% heat-inactivated fetal bovine serum, 1% penicillin–streptomycin, 20 ng ml<sup>-1</sup> murine granulocyte macrophage colony-stimulating factor and 5 ng ml<sup>-1</sup> interleukin-4). Half of the culture medium volume was refreshed on day 2. Non-adherent and loosely adherent immature BMDCs were collected on day 4, and we determined their phenotype by assessing CD11c expression (60–80% CD11c<sup>+</sup> cells were routinely obtained).

Tumor cells were treated with different agents (5  $\mu\text{M}$ ) for 6 h, and then the culture medium was replaced by fresh medium followed by further incubation for 36 h. Afterwards, the medium supernatant of tumor cells was collected and used to incubate BMDCs for 24 h before flow cytometry analysis.

### Immune cell and cytokine profiling

For immune cell profiling, peripheral blood monocytes (PBMCs), spleens, lymph nodes and tumors were harvested for assays. To isolate splenocytes, the spleens were mechanically homogenized and resuspended in red blood cell (RBC) lysis buffer (Solarbio, China) for RBCs removal. Tumors were cut into pieces and resuspended in medium containing collagenase D (1 mg ml<sup>-1</sup>, Sigma-Aldrich) followed by incubation in a shaking incubator for 30 min at 37 °C. After washing, suspensions of PBMCs, lymph node cells, splenocytes and tumor cells were stained with various antibodies. For memory T cell analysis, PBMCs, splenocytes and tumor cells were stained with Zombie Aqua™ (Biolegend, cat. no. 423102), blocked with CD16/32 antibody and further stained with fluorophore-labeled antibodies against CD45, CD3, CD4, CD8a, CD44, and CD62L at 4 °C. For dendritic cell analysis, BMDCs and lymph node cells were stained with Zombie Aqua™, blocked with CD16/32 antibody and further stained with fluorophore-labeled antibodies against CD45, CD11c, CD80, CD86, and MHC II at 4 °C. For OVA-specific T-cell analysis, splenocytes and tumor cells were stimulated by cell activation cocktail with brefeldin A (Biolegend, cat. no. 423304) at 37 °C for 6 h. Subsequently, cells were stained with Zombie Aqua™, blocked with CD16/32 antibody, and further stained with fluorophore-labeled antibodies against CD45, CD3, CD8a, IFN- $\gamma$ , and T-Select H-2K<sup>b</sup> OVA tetramer-SIINFELK-PE (MBL Life Science, cat. no. TS-5001-1C) at 4 °C. Then, the cells were washed twice with phosphate-buffered saline (PBS) and filtered through a 70- $\mu\text{m}$  nylon cell strainer before subjected to flow cytometry analysis.

### Cytokine detection

The plasma levels of IL12, TNF- $\alpha$ , and IFN- $\gamma$  were measured using ELISA kit (Novus Biologicals) according to the manufacturer's instructions. Plasma samples were obtained from the mice at predetermined days and diluted for analysis.

### In vivo prophylactic tumor vaccination study

We exposed 4T1 cells to distinct chemotherapeutic agents and induced -70%  $\pm$  10% cell death. Then, the dying 4T1 cells were subcutaneously injected into right flank of the immunocompetent BALB/c mice. Control mice received sterile saline instead of this cancer cell vaccine. After immunization with the corresponding cancer vaccines (containing 2  $\times$  10<sup>6</sup> cells in 100  $\mu\text{l}$  sterile phosphate-buffered saline) twice on day 0 and day 7, mice were then orthotopically rechallenged with 5  $\times$  10<sup>5</sup> live 4T1 cells into the fifth mammary fat pad on day 14. The tumor growth, metastasis and the survival rate were monitored throughout the whole study. On day 59, lymph nodes (axillary and inguinal), lungs and livers were collected from mice bearing established 4T1 tumors in each group, and subjected to H&E staining for tumor metastasis analysis. Immune profiling was performed by ELISA and flow cytometry analysis.

### In vivo tumor models

To test the specific abscopal antitumor effect, bilateral tumor models were established. Briefly, 1  $\times$  10<sup>6</sup> 4T1 tumor cells were subcutaneously

inoculated into both flanks of BALB/c mice, or  $1 \times 10^6$  4T1 cells and  $5 \times 10^5$  CT26 cells were subcutaneously inoculated into the right and left flanks of BALB/c mice, respectively. Seven days after tumor inoculation, intratumoral injection of mtDSN-2 ( $1 \text{ mg kg}^{-1}$ ) was performed on the right tumor every other day twice. The growth of tumors on both flanks was monitored at various time points. Representative tumors were harvested for immunofluorescence staining to assess CD8<sup>+</sup> T-cell infiltration on day 8. Mice were defined as dead and sacrificed when tumor volume exceeded  $1500 \text{ mm}^3$ .

To measure the effects on cancer metastasis, 4T1 tumor cells were transplanted into the right flank of BALB/c mice. When the resulting tumors reached  $\sim 150 \text{ mm}^3$ , the mice received intratumoral injections on day 0 and 2 of one of the treatment formulations: saline, mtDSN-2 ( $1 \text{ mg kg}^{-1}$ ), mtDSN-2 ( $1 \text{ mg kg}^{-1}$ ) plus MPLA ( $50 \mu\text{g kg}^{-1}$ ), and mtDSN-2 ( $1 \text{ mg kg}^{-1}$ ) plus anti-PD-1 ( $1 \text{ mg kg}^{-1}$ ). The tumor volume was monitored. Representative tumors were harvested for immunofluorescence staining to assess CD8<sup>+</sup> T-cell infiltration on day 8. Mice were sacrificed and lungs were collected when tumor volume exceeded  $1500 \text{ mm}^3$  or at the endpoint of the experiment. Metastatic burden of lungs was assessed on the basis of the H&E staining.

To assess the therapeutic effect on colorectal cancer,  $2 \times 10^6$  MC38 tumor cells were subcutaneously inoculated on C57BL/6 mice. Treatment started when the tumor volumes reached  $\sim 100 \text{ mm}^3$  with one of the formulations: saline (intratumoral), anti-PD-1 ( $10 \text{ mg kg}^{-1}$ , intraperitoneal), mtDSN-2 ( $1 \text{ mg kg}^{-1}$ , intratumoral), and mtDSN-2 ( $1 \text{ mg kg}^{-1}$ , intratumoral) plus anti-PD-1 ( $10 \text{ mg kg}^{-1}$ , intraperitoneal). On day 15, representative tumors were photographed and subjected to immunohistochemical analysis. For the MC38 rechallenge study, cured mice were subcutaneously injected with  $2 \times 10^6$  MC38 cells 67 days after the first injection of MC38 cells. Healthy mice received the same injection as a control. At the end of the experiment, PBMCs and splenocytes were collected for flow cytometry analysis.

To assess the antitumor effect on anti-PD-1-resistant tumors, mice bearing MC38 tumors were repeated administrated with anti-PD-1 antibodies at a low dose ( $5 \text{ mg kg}^{-1}$ ) followed by the serial transplantation of low-response tumors into different mice according to the indicated experiment schema. After three cycles of anti-PD-1-resistance induction, mice bearing anti-PD-1-resistant MC38 tumors were treated with one of the formulations: saline (intratumoral), anti-PD-1 ( $10 \text{ mg kg}^{-1}$ , intraperitoneal), mtDSN-2 ( $1 \text{ mg kg}^{-1}$ , intratumoral), and mtDSN-2 ( $1 \text{ mg kg}^{-1}$ , intratumoral) plus anti-PD-1 ( $10 \text{ mg kg}^{-1}$ , intraperitoneal). Tumor volume was monitored and the survival time was recorded. On day 15, representative tumors were photographed and subjected to immunohistochemical analysis. To build another anti-PD-1-resistant tumor model,  $1 \times 10^6$  CT26 tumor cells were subcutaneously inoculated into BALB/c mice. These mice underwent the same treatment protocol as MC38-bearing mice.

### Single-cell RNA sequencing

Mice bearing anti-PD-1-resistant MC38 tumors received intratumoral injections of vehicle (saline containing 5% DMSO) or mtDSN-2 ( $1 \text{ mg kg}^{-1}$ ) every 3 days. After a total of three doses, tumors were collected, minced and dissociated ( $n = 3$  mice or samples were pooled to control for biological variability). The cell suspension was prepared according to general protocols and loaded into Chromium microfluidic chips with 3' (v3.1) chemistry and barcoded with a 10X Chromium Controller (10X Genomics). RNA from the barcoded cells was subsequently reverse-transcribed. The sequencing libraries were constructed using a Chromium Single Cell 3' (v3.1) reagent kit (10X Genomics) (Novogene). Illumina NovaSeq 6000 PE150 was used for sequencing following the manufacturer's instructions. Raw reads were demultiplexed and mapped to the reference genome by 10X Genomics Cell Ranger pipeline using default parameters. After mapping with Cell Ranger (v7.0.0) on the mouse reference, downstream single-cell analyses were further performed using Seurat (v4.3.0). In silico doublet

prediction and removal were performed using DoubletFinder. Cells with number of genes detected per cell  $>8500$  or  $<200$ , and percentage of mitochondrial genes  $>30\%$  were removed from the dataset before the downstream analysis. After this initial filtering, we normalized the gene expression of each cell by the total expression before performing log-transformation. In the log-normalized data, we identified the top 2000 most highly variable genes and included them in principal component analysis and clustering analysis. Scaling was carried out by centering the expression of each gene before dividing the mean-centered expressions by the standard deviation. Cell cluster annotations were performed by manual annotation based on selected canonical markers via unsupervised clustering.

Based on filtered gene expression matrix by Seurat, differential expression analysis between samples was performed using the edgeR package for acquiring zone-specific marker genes. GO enrichment and KEGG pathway analyses of marker genes were conducted using the cluster Profiler R package, where gene length bias was corrected. GSEA was used to test for enrichment of a specific gene set. A normalized enrichment score (NES) was specified for each GSEA. For the differential gene-expression, a significant result was defined as an unadjusted  $P$  value lower than 0.05.

### Statistics and reproducibility

Graphs were generated and statistical analyses were performed using GraphPad Prism v.8 unless stated otherwise. The data are represented as mean  $\pm$  s.d., and values of  $P < 0.05$  were considered statistically significant. Comparison between two unpaired groups was performed using a two-tailed Student's  $t$  test. For multiple comparisons involving one variable, one-way ANOVA was used with Tukey's or Bonferroni's multiple comparison test when SDs were equal; Brown-Forsythe and Welch ANOVA with Dunnett's T3 multiple comparisons test was used when SDs were not equal. Two-way ANOVA with Tukey's or Sidak's multiple comparison test was used for simultaneous analysis of two variables (tumor growth over time) among multiple groups. Survival curves were obtained using the Kaplan-Meier method and compared by the log-rank test. Sample sizes of in vivo studies were designed based on previous experience of the experimental models, and thus no statistical method was used to predetermine sample size. Mice were randomized to different groups, carefully examined daily, and humanely euthanized at defined study endpoints. Data collection during experiments was performed blinded to ensure the consistency of measurements across all groups. No data were excluded from the analyses. Besides, the histological examination was performed blinded to avoid biased assessment.

### Reporting summary

Further information on research design is available in the Nature Portfolio Reporting Summary linked to this article.

### Data availability

The scRNA-seq datasets generated for this study have been deposited in the NCBI Gene Expression Omnibus (GEO) under accession number [GSE272255](https://www.ncbi.nlm.nih.gov/geo/query/acc.cgi?acc=GSE272255). The remaining data are available within the Article, Supplementary Information or Source Data file. Source data are provided with this paper.

### References

1. Topalian, S. L., Drake, C. G. & Pardoll, D. M. Immune checkpoint blockade: a common denominator approach to cancer therapy. *Cancer Cell* **27**, 450–461 (2015).
2. Borcoman, E. et al. Novel patterns of response under immunotherapy. *Ann. Oncol.* **30**, 385–396 (2019).
3. Fridman, W. H., Pages, F., Sautes-Fridman, C. & Galon, J. The immune contexture in human tumours: impact on clinical outcome. *Nat. Rev. Cancer* **12**, 298–306 (2012).

4. Joyce, J. A. & Fearon, D. T. T cell exclusion, immune privilege, and the tumor microenvironment. *Science* **348**, 74–80 (2015).
5. Galon, J. & Bruni, D. Approaches to treat immune hot, altered and cold tumours with combination immunotherapies. *Nat. Rev. Drug Discov.* **18**, 197–218 (2019).
6. Zappasodi, R., Merghoub, T. & Wolchok, J. D. Emerging concepts for immune checkpoint blockade-based combination therapies. *Cancer Cell* **33**, 581–598 (2018).
7. Jin, S. M. et al. A nanoadjuvant that dynamically coordinates innate immune stimuli activation enhances cancer immunotherapy and reduces immune cell exhaustion. *Nat. Nanotechnol.* **18**, 390–402 (2023).
8. Xian, S., Chen, X., Ren, S., Chen, X. & Wang, H. Ionizable STING-activating nanoadjuvants enhance tumor immunogenicity and potentiate immunotherapy efficacy in solid tumors. *Cancer Res.* <https://doi.org/10.1158/0008-5472.CAN-23-3511> (2024).
9. Krysko, D. V. et al. Immunogenic cell death and DAMPs in cancer therapy. *Nat. Rev. Cancer* **12**, 860–875 (2012).
10. Kroemer, G., Galluzzi, L., Kepp, O. & Zitvogel, L. Immunogenic cell death in cancer therapy. *Annu. Rev. Immunol.* **31**, 51–72 (2013).
11. Obeid, M. et al. Calreticulin exposure dictates the immunogenicity of cancer cell death. *Nat. Med.* **13**, 54–61 (2007).
12. Oresta, B. et al. Mitochondrial metabolic reprogramming controls the induction of immunogenic cell death and efficacy of chemotherapy in bladder cancer. *Sci. Transl. Med.* **13**, eaba6110 (2021).
13. Pfirschke, C. et al. Immunogenic chemotherapy sensitizes tumors to checkpoint blockade therapy. *Immunity* **44**, 343–354 (2016).
14. Vyas, S., Zaganjor, E. & Haigis, M. C. Mitochondria and cancer. *Cell* **166**, 555–566 (2016).
15. Weinberg, S. E., Sena, L. A. & Chandel, N. S. Mitochondria in the regulation of innate and adaptive immunity. *Immunity* **42**, 406–417 (2015).
16. Mills, E. L., Kelly, B. & O'Neill, L. A. J. Mitochondria are the powerhouses of immunity. *Nat. Immunol.* **18**, 488–498 (2017).
17. Yu, K. et al. A mitochondria-targeted NIR-II AIEgen induced pyroptosis for enhanced tumor immunotherapy. *Adv. Healthc. Mater.* **12**, e2301693 (2023).
18. Harel, M. et al. Proteomics of melanoma response to immunotherapy reveals mitochondrial dependence. *Cell* **179**, 236–250.e218 (2019).
19. Tigano, M., Vargas, D. C., Tremblay-Belzile, S., Fu, Y. & Sfeir, A. Nuclear sensing of breaks in mitochondrial DNA enhances immune surveillance. *Nature* **591**, 477–481 (2021).
20. Chen, C. et al. Massively evoking immunogenic cell death by focused mitochondrial oxidative stress using an AIE luminogen with a twisted molecular structure. *Adv. Mater.* **31**, e1904914 (2019).
21. Wang, H. X. et al. Self-assembling prodrugs by precise programming of molecular structures that contribute distinct stability, pharmacokinetics, and antitumor efficacy. *Adv. Funct. Mater.* **25**, 4956–4965 (2015).
22. Wang, H. X. et al. New generation nanomedicines constructed from self-assembling small-molecule prodrugs alleviate cancer drug toxicity. *Cancer Res.* **77**, 6963–6974 (2017).
23. Huang, L. L. et al. Quantitative self-assembly of photoactivatable small molecular prodrug cocktails for safe and potent cancer chemo-photodynamic therapy. *Nano Today* **36** (2021).
24. Xie, H. Y. et al. Target-oriented delivery of self-assembled immunosuppressant cocktails prolongs allogeneic orthotopic liver transplant survival. *J. Control. Release* **328**, 237–250 (2020).
25. Paggio, A. et al. Identification of an ATP-sensitive potassium channel in mitochondria. *Nature* **572**, 609–613 (2019).
26. LeBleu, V. S. et al. PGC-1 $\alpha$  mediates mitochondrial biogenesis and oxidative phosphorylation in cancer cells to promote metastasis (vol 16, pg 992, 2014). *Nat. Cell Biol.* **16**, 1125–1125 (2014).
27. Cassidy-Stone, A. et al. Chemical inhibition of the mitochondrial division dynamin reveals its role in Bax/Bak-dependent mitochondrial outer membrane permeabilization. *Dev. Cell* **14**, 193–204 (2008).
28. Arnoult, D. et al. Bax/Bak-dependent release promotes of DDP/TIMM8a promotes Drp1-mediated mitochondrial fission and mitoptosis during programmed cell death. *Curr. Biol.* **15**, 2112–2118 (2005).
29. Dierge, E. et al. Peroxidation of n-3 and n-6 polyunsaturated fatty acids in the acidic tumor environment leads to ferroptosis-mediated anticancer effects. *Cell Metab.* **33**, 1701–1715.e1705 (2021).
30. Sperandio, S., de Belle, I. & Bredesen, D. E. An alternative, non-apoptotic form of programmed cell death. *Proc. Natl Acad. Sci. USA* **97**, 14376–14381 (2000).
31. Mandula, J. K. et al. Ablation of the endoplasmic reticulum stress kinase PERK induces paraptosis and type I interferon to promote anti-tumor T cell responses. *Cancer Cell* **40**, 1145–1160.e1149 (2022).
32. Guo, B. et al. Humanin peptide suppresses apoptosis by interfering with Bax activation. *Nature* **423**, 456–461 (2003).
33. Wei, M. C. et al. Proapoptotic BAX and BAK: a requisite gateway to mitochondrial dysfunction and death. *Science* **292**, 727–730 (2001).
34. Ow, Y. P., Green, D. R., Hao, Z. & Mak, T. W. Cytochrome c: functions beyond respiration. *Nat. Rev. Mol. Cell Biol.* **9**, 532–542 (2008).
35. Lang, S. et al. An update on Sec61 channel functions, mechanisms, and related diseases. *Front. Physiol.* **8**, 887 (2017).
36. Porter, A. G. & Jänicke, R. U. Emerging roles of caspase-3 in apoptosis. *Cell Death Differ.* **6**, 99–104 (1999).
37. Gardai, S. J. et al. Cell-surface calreticulin initiates clearance of viable or apoptotic cells through trans-activation of LRP on the phagocyte. *Cell* **123**, 321–334 (2005).
38. Scaffidi, P., Misteli, T. & Bianchi, M. E. Release of chromatin protein HMGB1 by necrotic cells triggers inflammation. *Nature* **418**, 191–195 (2002).
39. Elliott, M. R. et al. Nucleotides released by apoptotic cells act as a find-me signal to promote phagocytic clearance. *Nature* **461**, 282–U165 (2009).
40. Wozny, M. R. et al. In situ architecture of the ER-mitochondria encounter structure. *Nature* **618**, 188–192 (2023).
41. Giorgi, C., De Stefani, D., Bononi, A., Rizzuto, R. & Pinton, P. Structural and functional link between the mitochondrial network and the endoplasmic reticulum. *Int. J. Biochem. Cell Biol.* **41**, 1817–1827 (2009).
42. Inagi, R., Ishimoto, Y. & Nangaku, M. Proteostasis in endoplasmic reticulum-new mechanisms in kidney disease. *Nat. Rev. Nephrol.* **10**, 369–378 (2014).
43. Guo, X. et al. Mitochondrial stress is relayed to the cytosol by an OMA1-DELE1-HRI pathway. *Nature* **579**, 427–432 (2020).
44. Obeid, M. et al. Leveraging the immune system during chemotherapy: moving calreticulin to the cell surface converts apoptotic death from “silent” to immunogenic. *Cancer Res.* **67**, 7941–7944 (2007).
45. Fucikova, J. et al. Human tumor cells killed by anthracyclines induce a tumor-specific immune response. *Cancer Res.* **71**, 4821–4833 (2011).
46. Tesniere, A. et al. Immunogenic death of colon cancer cells treated with oxaliplatin. *Oncogene* **29**, 482–491 (2010).
47. Fitzgerald, K. A. & Kagan, J. C. Toll-like receptors and the control of immunity. *Cell* **180**, 1044–1066 (2020).
48. Sun, L. J. et al. Activating a collaborative innate-adaptive immune response to control metastasis. *Cancer Cell* **39**, 1361–1374 (2021).
49. Hsu, R. Y. C. et al. LPS-induced TLR4 signaling in human colorectal cancer cells increases  $\beta$ 1 integrin-mediated cell adhesion and liver metastasis. *Cancer Res.* **71**, 1989–1998 (2011).

50. Ran, S. The role of TLR4 in chemotherapy-driven metastasis. *Cancer Res.* **75**, 2405–2410 (2015).
  51. Albregues, J. et al. Neutrophil extracellular traps produced during inflammation awaken dormant cancer cells in mice. *Science* **361**, eaao4227 (2018).
  52. Efremova, M. et al. Targeting immune checkpoints potentiates immunoeediting and changes the dynamics of tumor evolution. *Nat. Commun.* **9**, 32 (2018).
  53. Schoenfeld, A. J. & Hellmann, M. D. Acquired resistance to immune checkpoint inhibitors. *Cancer Cell* **37**, 443–455 (2020).
  54. Corcoran, R. B. & Grothey, A. Efficacy of immunotherapy in microsatellite-stable or mismatch repair proficient colorectal cancer—fact or fiction? *JAMA Oncol.* **6**, 823–824 (2020).
  55. Castle, J. C. et al. Immunomic, genomic and transcriptomic characterization of CT26 colorectal carcinoma. *BMC Genom.* **15**, 190 (2014).
  56. Andreatta, M. et al. Interpretation of T cell states from single-cell transcriptomics data using reference atlases. *Nat. Commun.* **12**, 2965 (2021).
  57. Davidson, S. et al. Fibroblasts as immune regulators in infection, inflammation and cancer. *Nat. Rev. Immunol.* **21**, 704–717 (2021).
  58. Cassetta, L. & Pollard, J. W. Tumor-associated macrophages. *Curr. Biol.* **30**, R246–R248 (2020).
  59. Jaillon, S. et al. Neutrophil diversity and plasticity in tumour progression and therapy. *Nat. Rev. Cancer* **20**, 485–503 (2020).
  60. Nakahira, K. et al. Autophagy proteins regulate innate immune responses by inhibiting the release of mitochondrial DNA mediated by the NALP3 inflammasome. *Nat. Immunol.* **12**, 222–230 (2011).
  61. West, A. P. et al. Mitochondrial DNA stress primes the antiviral innate immune response. *Nature* **520**, 553–557 (2015).
  62. West, A. P. et al. TLR signalling augments macrophage bactericidal activity through mitochondrial ROS. *Nature* **472**, 476–U543 (2011).
  63. Alissafi, T. et al. Mitochondrial oxidative damage underlies regulatory T cell defects in autoimmunity. *Cell Metab.* **32**, 591–604.e597 (2020).
  64. Buck, M. D. et al. Mitochondrial dynamics controls T cell fate through metabolic programming. *Cell* **166**, 63–76 (2016).
  65. Ron-Harel, N. et al. Mitochondrial biogenesis and proteome remodeling promote one-carbon metabolism for T cell activation. *Cell Metab.* **24**, 104–117 (2016).
  66. Rohrbach, S. Effects of dietary polyunsaturated fatty acids on mitochondria. *Curr. Pharm. Des.* **15**, 4103–4116 (2009).
  67. Galluzzi, L., Buque, A., Kepp, O., Zitvogel, L. & Kroemer, G. Immunogenic cell death in cancer and infectious disease. *Nat. Rev. Immunol.* **17**, 97–111 (2017).
  68. Giese, M. A., Hind, L. E. & Huttenlocher, A. Neutrophil plasticity in the tumor microenvironment. *Blood* **133**, 2159–2167 (2019).
  69. Kolaczowska, E. & Kubers, P. Neutrophil recruitment and function in health and inflammation. *Nat. Rev. Immunol.* **13**, 159–175 (2013).
  70. Gebhardt, C., Nemeth, J., Angel, P. & Hess, J. S100A8 and S100A9 in inflammation and cancer. *Biochem. Pharmacol.* **72**, 1622–1631 (2006).
  71. Cha, J. H., Chan, L. C., Li, C. W., Hsu, J. L. & Hung, M. C. Mechanisms controlling PD-L1 expression in cancer. *Mol. Cell* **76**, 359–370 (2019).
- technical assistance on TEM and SEM analysis. We thank Chun Guo from the Core Facilities, Zhejiang University School of Medicine for her technical support. This work was supported by grants from National Natural Science Foundation of China (82303786 to L.R., 82303561 to J.W., 82273490, 82073296 and 81773193 to H.W.), China Postdoctoral Science Foundation (2023M733081 to L.R.), China National Postdoctoral Program for Innovative Talents (BX20230313 to J.W.), Non-profit Central Research Institute Fund of Chinese Academy of Medical Sciences (2023-PT320-02 to H.W.), Natural Science Foundation of Shandong Province (ZR2023ZD59 to H.W.), Research Project of Jinan Microecological Biomedicine Shandong Laboratory (JNL-2022010B to H.W.), and Zhejiang Provincial Natural Science Foundation of China (LR19H160002 to H.W.).

## Author contributions

L.R. and H.W. conceived and designed research; L.R. performed experiments; J.W., X.L., J.Y., Y.M., and F.M. helped to perform the research; L.R., J.W., S.Z., W.H., and H.W. interpreted and analyzed the data; L.R. S.Z., W.H., and H.W. wrote and revised the manuscript. All authors discussed the results and commented on the paper.

## Competing interests

The authors declare no competing interests.

## Additional information

**Supplementary information** The online version contains supplementary material available at <https://doi.org/10.1038/s41467-024-51945-y>.

**Correspondence** and requests for materials should be addressed to Shusen Zheng, Weidong Han or Hangxiang Wang.

**Peer review information** *Nature Communications* thanks the anonymous reviewer(s) for their contribution to the peer review of this work. A peer review file is available.

**Reprints and permissions information** is available at <http://www.nature.com/reprints>

**Publisher's note** Springer Nature remains neutral with regard to jurisdictional claims in published maps and institutional affiliations.

**Open Access** This article is licensed under a Creative Commons Attribution-NonCommercial-NoDerivatives 4.0 International License, which permits any non-commercial use, sharing, distribution and reproduction in any medium or format, as long as you give appropriate credit to the original author(s) and the source, provide a link to the Creative Commons licence, and indicate if you modified the licensed material. You do not have permission under this licence to share adapted material derived from this article or parts of it. The images or other third party material in this article are included in the article's Creative Commons licence, unless indicated otherwise in a credit line to the material. If material is not included in the article's Creative Commons licence and your intended use is not permitted by statutory regulation or exceeds the permitted use, you will need to obtain permission directly from the copyright holder. To view a copy of this licence, visit <http://creativecommons.org/licenses/by-nc-nd/4.0/>.

© The Author(s) 2024

## Acknowledgements

We thank Chenyu Yang, Yuchen Zhang and Dandan Song in the Center of Cryo-Electron Microscopy (CCEM), Zhejiang University for their